First evidence of the trisulfur radical ion S3- and other sulfur polymers in natural fluid inclusions

Guillaume Barré, Laurent Truche, Elena Bazarkina, Raymond Michels, Jean Dubessy

First evidence of the trisulfur radical ion S_3^- and other sulfur polymers in natural fluid inclusions

Guillaume Barré[1*], Laurent Truche[1,2], Elena F. Bazarkina[1,3,4], Raymond Michels[1], Jean Dubessy[1]

[1]*Université de Lorraine, CNRS, GeoRessources, UMR 7359, BP 70239, F-54506 Vandoeuvre-lès-Nancy, France*

[2]*Université Grenoble Alpes, CNRS, ISTerre, UMR 5275, BP 53, 38041 Grenoble, France*

[3]*Institute of Geology of Ore Deposits, Mineralogy, Petrography and Geochemistry, Russian Academy of Sciences, IGEM RAS, Staromonetny per. 35, 119017 Moscow, Russia*

[4]*Inst. Néel, UPR 2940 CNRS - Univ. Grenoble Alpes, F-38000 Grenoble, France*

[*]*e-mail: guillaume.barre@univ-lorraine.fr*

Abstract

Sulfur plays a key role in numerous processes occurring in the Earth's crust. However, its speciation in deep and hot geological fluids remains poorly constrained. Here, we used quantitative *in-situ* Raman spectroscopy on natural fluid inclusions from deep sedimentary environments where thermochemical sulfate reduction (TSR) occurred to determine the sulfur speciation at temperatures representative of their entrapment conditions (100-300°C). Results unambiguously demonstrate the presence of the trisulfur ion S_3^- and other polymeric S species (S_n^{2-} ±S_n^0) at temperature (T) > 100°C, whereas only sulfide and sulfate were detected at 25°C. From 200 to 300°C, sulfate and sulfide, the two dominant S species, contribute to 41 ± 9 % and 59 ± 9 % of the mean total dissolved S concentration ([S_{tot}] = 0.25 mol/kg$_{H2O}$ = 0.8 wt%), respectively. The S_3^- concentration accounts for 0.2 to 3 % of S_{tot} in this T range, with a

maximum recorded concentration of 2.9×10^{-2} mol/kg_{H2O} (2780 ppm) at 300°C. This observation implies that the TSR process occurs under physico-chemical conditions that enhanced the stability of S_3^- and other polymeric S species. This conclusion has important consequences for the genesis of base metal sulfide deposits and sour gas fields where reduced sulfur originates from TSR.

Keywords: S_3^-; Fluid inclusion; Raman spectroscopy; Sulfur speciation; Thermochemical Sulfate Reduction

1. Introduction

Sulfur speciation and concentration in deep basinal brines play a crucial role in the formation of sour (H_2S-bearing) gas field (Orr, 1974; Worden and Smalley, 1996; Machel, 2001; Walters et al., 2015; Cai et al., 2016) and the genesis of many sedimentary-hosted ore deposits (Heydari and Moore, 1989; Basuki et al., 2008; Thom and Anderson, 2008). One of the most important reactions controlling the sulfur behavior in deep sedimentary environments is the abiogenic reduction of sulfate to sulfide coupled with the oxidation of hydrocarbons, which is termed thermochemical sulfate reduction (TSR). This reaction occurs at temperature above 100-140°C and is under strong kinetic control (Kiyosu and Krouse, 1993; Goldhaber and Orr, 1995; Cross et al., 2004; Thom and Anderson, 2008; Zhang et al., 2008; Truche et al., 2009; Yuan et al., 2013). The sulfur speciation has also a major impact on the rate and extent of TSR, because both the reactivity of dissolved sulfate compounds (e.g. SO_4^{2-}, HSO_4^-, $CaSO_4^0$, $MgSO_4^0$) and the relative stability of intermediate valence sulfur species (e.g. thiosulfate, polysulfides, labile organic sulfur compounds) drive the electron transfer from S^{+6} to S^{2-} (Goldstein and Aizenshtat, 1994; Cai et al., 2003; Amrani et al., 2008; Ma et al., 2008; Gvirtzman et al., 2015). Most of our knowledge of sulfur speciation in saline brines from deep burial diagenetic environments relies

on measurements made on quenched fluids from surface springs, water/oil production wells, and fluid inclusions entrapped in minerals. Sulfate and sulfide are the dominant dissolved sulfur species in these environments, with concentrations up to 0.5 mol/kg_{H2O} (Boiron et al., 1999; Horita et al., 2002; Worden et al., 2003). Other intermediate valence sulfur species such as sulfite (SO_3^-), thiosulfate ($S_2O_3^{2-}$), polythionates ($S_nO_6^{2-}$), polysulfides (S_n^{2-}) or dissolved elemental sulfur (S^0) have been found in surface hydrothermal springs, and sulfide rich water well (Boulègue, 1978; Takano, 1987; Webster, 1987; Veldeman et al., 1991; Takano et al., 1994; Xu et al., 1998; Kamyshny et al., 2008; Nordstrom et al., 2009; Kaasalainen and Stefánsson, 2011). However, their speciation and concentration may not reflect the true sulfur chemistry in deep geological fluids that is known to be very sensitive to temperature (T), pressure (P), redox, and pH conditions (Giggenbach, 1974; Ohmoto and Lasaga, 1982; Barnes, 1997).

The recent discovery of the trisulfur ion S_3^- in aqueous S-rich fluids from laboratory experiments using *in-situ* Raman spectroscopy at T > 200°C, acidic-to-neutral pH (2-6), and redox condition enabling coexistence of sulfate and sulfide has challenged our interpretation of sulfur behavior in hydrothermal fluids (Pokrovski and Dubrovinsky, 2011; Chivers and Elder, 2013; Jacquemet et al., 2014; Truche et al., 2014; Pokrovski and Dubessy, 2015). Nevertheless, little attention has been given to the sulfur speciation in natural geological fluids, and the concentration of intermediate sulfur species at relevant T-P is unknown. To our knowledge there is no study on sulfur speciation in natural fluid inclusions at elevated T.

Here, we performed quantitative *in-situ* analysis of sulfur speciation in well-preserved natural fluid inclusions from a geological setting where TSR occurred. We used *in-situ* Raman spectroscopy coupled to a heating stage to analyze samples under temperatures representative of their entrapment conditions.

2. Geological setting

For the purpose of this study, rock samples were selected from the Carnian evaporites (upper Triassic), named "gypse nappe" formation, outcropping in the Arc Valley (French Alps), between Modane and Sollières-l'Envers (Fig. 1). This geological formation exposes to the surface a world-class evidence of TSR occurrence in previously deeply buried evaporites, with coexistence of sulfate (anhydrite), sulfide (pyrite), and native sulfur at both macro (Fig. 2) and microscopic scale (not shown). The Carnian evaporites belong to the Triassic formation marking a major Alpine structural discontinuity between the Permian basement and the allochtonous Piedmont unit of Cretaceous age (Fig. 1, see also Debelmas et al., 1989a; Strzerzynski et al., 2012 and reference therein). They are characterized by massive anhydrite embedding dolomite layers and smaller intercalations of micaschist. Elemental sulfur occurs as vugs within the anhydrite or associated to the white well-crystallized dolomite as fracture infillings within the brownish cryptocrystalline dolomite layers. Fluorite and quartz crystals (mm to cm in size) are also found disseminated within the anhydrite or the brownish cryptocrystalline dolomite (Fig. 2b). The Carnian formation is tectonically deformed. Anhydrite shows schistosity and folding while dolomite shows boudinage levels from still recognizable layers to totally isolated blocs. The formation has been affected by the Modane-Aussois metamorphic event that recorded an isothermal exhumation during the Paleogene. The peak of metamorphism led to maximum temperature and pressure around 350°C and 7.5 kbar (Gabalda et al., 2009; Lanari et al., 2012; Strzerzynski et al., 2012). The fluid inclusions studied here are preferentially located in the anhydrite ± quartz ± fluorite veins that intersect the dolomitic "boudins", and are distributed in plane, clusters or as isolated inclusions. They do not display any deformation. These textural

features strongly suggest that the fluid inclusions were trapped during the retrograde metamorphic pathway under brittle conditions, and not during the prograde pathway.

3. Samples and methods

3.1. Choice of the host mineral

The natural fluid inclusions studied here are hosted in quartz, fluorite or anhydrite. Quartz and fluorite minerals are present as small crystals (100 μm to 1 cm of diameter) embedded in the anhydrite matrix. Fluorite is the best host mineral to study sulfur speciation by Raman spectroscopy, because of the absence of peaks overlap between fluorite and sulfur species. However, thermal dilatation of fluorite may slightly change the liquid-vapor ratio in the fluid inclusion (Bodnar and Bethke, 1984) and therefore change the sulfur speciation at elevated T. Having in mind this limitation, and despite the fact that the evolution of sulfate and sulfide concentration in quartz hosted fluid inclusions are identical within errors to those measured in fluorite, we advise the reader that our quantitative concentration measurements of the various sulfur species concentration in fluorite-hosted fluids inclusions at T above 200°C are given for indicative purpose. Quartz has a lower thermal expansion than fluorite, but it has some Raman peaks in the low wavenumber region that may hide the potential presence of polymeric sulfur species. No fluid inclusions hosted in anhydrite were retained for sulfur speciation investigations, owing to numerous peaks overlap between the host mineral and the dissolved sulfur species.

3.2. Fluid inclusions analysis

A total of 72 fluid inclusions from 3 different outcrops located in the Arc Valley (Fig. 1 and Supplementary Table S1 and S2) were analyzed by microthermometry, Raman spectrometry, and Fourier Transform Infrared spectrometry (FTIR, specific details in the Supplementary material). The salinities and homogenization temperatures (T_h) of the fluid inclusions were obtained by

114 microthermometry and Raman spectroscopy. Raman analyses were performed at 25-300°C using
115 a heating stage in order to study *in-situ* the composition of the trapped paleofluids. External
116 standard solutions of HSO_4^-, SO_4^{2-}, and $H_2S_{(aq)}$ were performed to establish Raman calibration
117 coefficients allowing quantitative analysis of each of these sulfur forms. Calibration coefficients
118 of S_3^- were derived from Pokrovski and Dubessy (2015). The complete analytical procedure is
119 described below.
120 *3.2.1. Microthermometric analysis*
121 Microthermometric measurements were performed on a Linkam THMSG600 heating-cooling
122 stage connected to an Olympus BX51 microscope allowing the analysis of fluid inclusions above
123 5 µm in size. Homogenization temperatures and salinities were deduced from these
124 measurements. The stage was calibrated using natural and synthetic fluid inclusion standards
125 with the following phase transitions: the melting temperature of a CO_2 ± Ar mixture at -56.9°C,
126 the ice melting and the critical homogenization temperatures of pure H_2O at 0.0 and 374.0°C,
127 respectively. According to the calibration curves, temperatures of phase changes have an
128 accuracy of about ±0.1°C for ice melting and ±1°C for total homogenization.
129 The composition of fluid inclusions in the H_2O–NaCl–$CaCl_2$ system was calculated using the
130 Microsoft Excel-based calculation sheet of Steele-MacInnis et al. (2011). We used the
131 combination of the measured temperatures of the final dissolution of halite and dissociation of
132 hydrates, hydrohalite ($NaCl \cdot 2H_2O$) or antarcticite ($CaCl_2 \cdot 6H_2O$), as input parameters.
133 All studied fluid inclusions homogenize into the liquid phase. Total homogenization
134 temperatures (T_h) were measured in fluid inclusions hosted in quartz. Fluorite and anhydrite-
135 hosted fluid inclusions are not suitable for T_h measurements because of the deformation of the
136 crystal, and change of the internal volume of the inclusion upon heating (Bodnar and Bethke,

1984; Vanko and Bach, 2005). However, their T_h are also given in Fig. 3 and Table S1 for indicative purpose.

The fluid inclusions liquid-vapor ratio was estimated on two-dimensional sections by measurements of the greatest area fraction for liquid and vapor phase for each fluid inclusion using ImageJ (free software at http://rsb.info.nih.gov).

3.2.2. Raman spectra acquisition

Raman spectra were recorded at the GeoRessources laboratory (Nancy, France) with a Labram HR spectrometer (®Jobin-Yvon, Horiba) coupled with a heating-stage dedicated to fluid inclusion (®Linkam, THMS-600) or capillary (®Linkam, CAP 500) studies. Raman spectra were mainly obtained using the 514 nm (green) Ar^+ laser excitation, with a laser power of 200 mW implying a maximal laser power at the sample around 20 mW. Some spectra were also recorded at lower laser power (0.7 to 7 mW at the sample) using filters, and compared with the full power spectra to ensure the absence of laser-induced phenomena such as sample overheating or photochemical reaction. Some spectra were also obtained with the 488 nm (blue) line of the Ar^+ laser for a better identification of sulfur species exhibiting Raman resonance phenomena such as S_3^-, S_n^{2-} or S_n^0 ions (Steudel, 2003). As demonstrated by Pokrovski and Dubessy (2015), the use of multiple excitation wavelengths allows more robust identification and quantification of sulfur species that exhibit Raman resonance phenomena, such as S_3^-, because their Raman signal is selectively enhanced at specific laser wavelengths, whereas that of non-resonant species such as sulfate and sulfide is little affected.

The spectrometer was calibrated using the Raman stretching vibrations of a Si wafer (520.7 cm^{-1} at 20°C), and oxygen (1555 cm^{-1}) and nitrogen (2331 cm^{-1}) gas from the air. The acquisition was performed using a grating of 1800 lines/mm, a slit width of 200 µm and a confocal hole of 500 µm providing a spectral resolution of 0.5 to 1 cm^{-1}. Spectral acquisition was collected with a

time of 15 to 60 s per spectral window and 2 to 4 accumulations in the wavenumber interval 100 to 4200 cm^{-1}. The use of an Olympus 100× objective coupled to the Raman spectrometer, allowed the identification of the different phases (solid, liquid and vapor) present in the fluid inclusions and to analyze them with a 1 μm laser spot size on the sample. In addition, the focus was tuned to optimize the intensity of the water O-H stretching band between 2800 and 3700 cm^{-1}. The ratio of the area of a Raman band of an aqueous solute to the OH stretching band of water is proportional to the solute concentration in the molarity scale at each temperature. Raman spectra were processed using the LabSpec 5.64.15 software (®Jobin-Yvon, Horiba). This software allows the baseline-subtraction and peak integration with a combination of Lorentzian and Gaussian functions (pseudo-Voigt function) to determine precisely the frequency position and the integrated peak area.

The samples were further heated step-by-step up to 300°C by steps of 50°C. Each analysis was performed after at least 15 minutes of down time at each step to allow the system to equilibrate. The duration of Raman measurements carried out at 100°C and 300°C was increased to 2 hours to ensure that a steady state was established. Salinities were also determined by Raman spectroscopy according to the technique developed by Dubessy et al. (2002) and Caumon et al. (2013), which is based on the deformation of the water stretching vibration band.

3.3. Raman spectra calibration

Sulfate (SO_4^{2-}), hydrogen sulfate (HSO_4^-), and hydrogen sulfide ($H_2S_{(aq)}$) concentration in the liquid phase present in the fluid inclusions was derived using calibration equations established from measurements in standard solutions (see Supplementary material for details on the calibration procedure). Each standard solution was loaded in fused silica capillary capsule (FSCC) purchased from Polymicro Technologies, LLC. This cell enables *in-situ* Raman

184 measurements up to ~500°C and ~2 kbar (Chou et al., 2008; Truche et al., 2014; Pokrovski and
185 Dubessy, 2015). It consists of round cross section silica-fused capillary tubing of 360 µm
186 external and 100 µm internal diameters. The capillary is sealed at both ends with a micro-torch
187 under vacuum and with frozen solution inside the capillary. The cell was heated step-by-step up
188 to 300°C on a heating-stage (®CAP-500 Linkam) which ensure a very good thermal stability
189 (±1°C) and negligible temperature gradients (<1°C over the cell length of 10-15 mm). To
190 increase the accuracy of concentration determination, the calibration solutions were measured
191 and processed identically to the fluid inclusions to establish calibration relationships allowing
192 quantitative analysis of SO_4^{2-}, HSO_4^-, and $H_2S_{(aq)}$. In addition, the effect of salinity on the
193 calibration was evaluated at three different NaCl concentrations: 0, 3 and 5 molar. To allow
194 quantitative comparisons of Raman peak areas in the liquid phase at different temperatures, the
195 spectra were normalized to the O-H stretching band of water between 2800 and 3700 cm^{-1}. We
196 used the linear relationship between the concentration of each species (C_i, mol/L) at given
197 temperature and its H_2O-normalized Raman peak area (A_i) given by Pokrovski and Dubessy
198 (2015) to determine calibration coefficients of the major sulfur species:

199 $$C_i = k_i(T) \times A_i \quad (1)$$

200 where k_i is the calibration coefficient for sulfate, hydrogen sulfate and $H_2S_{(aq)}$ at a given T (Fig.
201 4a and Supplementary Table S6). Equation 2 was then applied to convert the corresponding
202 species concentration to molality units:

203 $$m_i = (C_i/\rho_{fluid}) \times F \quad (2)$$

204 where m_i is the molality of sulfate, hydrogen sulfate or $H_2S_{(aq)}$ (in mol/kg_{H2O}), C_i, their
205 corresponding volumetric concentration (in mol/L), ρ_{fluid} the density (in g/cm^3) of aqueous liquid

206 at given T and P, and F, the molinity to molality conversion factor, F = 1000/(1000-W), where W
207 is the mass in grams of total dissolved solutes per 1 kg of liquid fluid.

208 As there is no standard for S_3^-, the kS_3^- coefficient was calculated in the 200-300°C
209 temperature range assuming the same temperature dependence as for the corresponding H_2S
210 coefficient (see Supplementary material for details) according to:

211 $$k_{S3-}(T) = k_{S3-}(500°C) \times k_{H2S}(T) / k_{H2S}(500°C) \quad (3)$$

212 with kS_3^- (500°C) = 0.020 ± 0.002 mol/L and k_{H2S} (500°C) = 15.8 ± 1 mol/L calculated from
213 Pokrovski and Dubessy (2015) (Fig. 4b; Supplementary Table S7).

214 The empirical Raman calibrations established on standards measured in the silica capillary
215 are perfectly applicable to our natural fluid inclusions for the following reasons: i) there is no
216 significant difference in refraction index between quartz (n = 1.544) and fused silica glass (n =
217 1.458), ii) the normalization of the Raman peaks area to the water stretching band avoids any
218 effect of sample geometry on the signal transmission, iii) the standards and the fluid inclusions
219 were processed identically (same configuration of the Raman spectrometer for signal
220 acquisition), iv) our standard solutions have salinity similar to that of the fluid inclusions, so the
221 effect of chlorinity on the shape/area of the water stretching band use to normalize the spectra is
222 accounted for.

223 The calibration coefficients reported here for sulfate, sulfide and S_3^-, combined with the
224 quantification limits for the Raman peak integrated area allow quantitative analysis down to
225 0.02; 0.01 and 0.0001 mol/kg_{H2O} respectively. The detection limits for these species is about 10
226 times lower than the quantification limits. The overall uncertainties of the reported
227 concentrations for S-species in the fluid inclusions are between 5 and 30% of the value
228 depending on the calibration coefficient uncertainties and the signal-to-noise ratio, as estimated

by fitting multiple spectra acquired at the same T-P at steady state, or using different baseline choices and normalized peak areas.

4. Results

4.1. Fluid inclusions characterization

At 25°C, all studied fluid inclusions contain several phases: aqueous liquid, gas, spherules of native sulfur, and crystals of halite. All fluid inclusions display similar salinities (25 ± 4 wt% eq. NaCl, with three times more NaCl than $CaCl_2$) and fluid composition (Supplementary Table S1 and S2). T_h values ranged from 98 to 355° C, with a quasi-gaussian distribution centered at 176°C (Fig. 3).

Fluid inclusions composition at room temperature (25±2°C) was analyzed by Raman spectroscopy for each phase present: vapor, liquid and solids (Fig. 5). The vapor phase (Fig. 5a, b) is dominated by CO_2 and H_2S as shown by their intense C-O and S-H stretching vibrations respectively at 1282-1386 cm^{-1} and 2603 cm^{-1}. These two gases are the by-products of TSR according to the general reaction:

$$SO_4^{2-} + CH_4 + 2H^+ = H_2S + CO_2 + 2H_2O \qquad (4)$$

Minor amount of N_2 ($\upsilon_{N\text{-}N}$ at 2330 cm^{-1}), CH_4 ($\upsilon_{C\text{-}H}$ at 2916 cm^{-1}) and H_2 ($\upsilon_{H\text{-}H}$ at 4154 cm^{-1}) are also detected. The presence of H_2 in the vapor phase of the fluid inclusions implies both very limited diffusion of H_2 and no or very poor post-entrapment modifications. The diffusion of H_2, into and out of fluid inclusion has already been described at temperature above 450°C (Mavrogenes and Bodnar, 1994), but such high temperature has never been reached in our geological context. The presence of both CH_4 and H_2 indicates that the reducing conditions were preserved. The N-N stretching vibration of N_2 presents two peaks (at 2330 cm^{-1} and 2327 cm^{-1}). The first one is due the presence of air along the path of the laser between the sample and the

252 microscope. The second one, more intense and slightly shifted to lower wavenumbers, is a clear
253 indication of the presence of N_2 under pressure inside the fluid inclusion (Wang and Wright,
254 1973).

255 The aqueous liquid phase is characterized by the broad O-H stretching band of water at
256 2800-3700 cm^{-1}. SO_4^{2-}, H_2S and HS^- are ubiquitous dissolved sulfur species in the aqueous phase
257 of the fluid inclusions (Fig. 5c, d) as indicated by their most intense Raman peaks at ~980 cm^{-1},
258 ~2590 cm^{-1} and ~2570 cm^{-1}, respectively. Hydrogen sulfate (HSO_4^-) characterized by the S-O
259 and S-OH stretching modes at ~1050 cm^{-1} and ~860 cm^{-1}, respectively, is not observed in the
260 fluid inclusions at 25°C. Dissolved CO_2 and, to a lesser extent, HCO_3^- are also identified by their
261 C-O stretching vibrations at 1380 and 1015 cm^{-1}, respectively. Another important feature
262 observed in the liquid phase is a small peak at 875 cm^{-1}. This band belongs to the B-O stretching
263 vibrations of boric acid $B(OH)_3$ (Servoss and Clark, 1957). Salinity values measured by Raman
264 spectroscopy (25 ± 2 wt% eq. NaCl) are similar to those derived by microthermometry.

265 In addition, the fluid inclusions contain spherule of elemental sulfur clearly identified by the
266 characteristic features of the S_8 ring molecules at ~150 (S-S bend), ~219 (S-S bend) and ~470 (S-
267 S stretch) cm^{-1} (Fig. 5e, f). In some rare occasions, tiny crystals of celestine ($SrSO_4$), anhydrite
268 ($CaSO_4$) and calcite ($CaCO_3$) are also observed in fluid inclusions hosted in fluorite only. A
269 comparison with the RRUFF reference (RRUFF database, http://rruff.info/) is shown in Fig. 5e,
270 f, g. The presence of these weakly soluble sulfate minerals together with the high detection limit
271 for dissolved sulfates (0.002 mol/kg_{H2O}; Dubessy et al., 1982) explain the fact that SO_4^{2-} is not
272 always detected in fluorite-hosted fluid inclusions.

273 Fourier Transform Infrared spectroscopy (FTIR) was also performed on some fluid
274 inclusions in order to identify potential organic compounds. The typical vibrations of a CH_2

functional group at 2849 and 2920 cm^{-1} are clearly visible on the spectra displayed in Supplementary Fig. S1. They may indicate the presence of a dissolved organic compound, but the absence of other characteristic vibrations prevents a better identification.

4.2. Sulfur speciation at elevated temperatures

Below 100°C, the Raman spectra show no changes with heating, even after 2 hours of continuous heating. At 100°C, native sulfur spherules begin to dissolve according to its disproportionation reaction under hydrothermal conditions yielding mainly sulfate and sulfide:

$$4S_{(s)} + 4H_2O = H^+ + HSO_4^- + 3H_2S_{(aq)} \quad (5)$$

Simultaneously, a new Raman band appears at 532 cm^{-1} and increases in intensity upon heating up to 300°C in the liquid phase of fluid inclusions (Fig. 6). This main peak is associated with resonant higher-order overtones 2ν, 3ν and 4ν at 1068, 1608, 2133 cm^{-1}. These characteristic features correspond without ambiguity to the resonance spectrum of the trisulfur S_3^- ion induced by the enhanced symmetric S-S stretching vibration (Pokrovski and Dubrovinsky, 2011). The trisulfur ion S_3^- is unambiguously identified by the main S-S symmetric bending (δ) vibration at ~240 cm^{-1} and stretching (ν) vibration at ~532 cm^{-1}, in agreement with previous work (Pokrovski and Dubrovinsky, 2011; Chivers and Elder, 2013; Pokrovski and Dubessy, 2015). Because S_3^- absorbs at ~600 nm, it exhibits a resonance Raman phenomenon with laser frequencies close to its absorption wavelength (Ar+, 514 nm). The characteristic progression of the overtones δ+ν, 2ν, 3ν, 4ν, 5ν and even 6ν (~780, 1070, 1600, 2130, 2665 and 3198 cm^{-1}, respectively), is clearly visible in all Raman spectra recorded at T ≥100°C (Fig. 6).

Another important Raman feature clearly visible in the liquid phase is a broad peak at 407 cm^{-1} with a shoulder at 440 cm^{-1}, accompanied by another poorly resolved band at 800-850 cm^{-1}

(Fig. 6a, c), which increases in intensity from 150 to 300°C. These Raman bands belong to S-S stretching vibrations (Steudel, 2003). All these features are better visible with the blue laser (488 nm) because of the much lower overlapping with the $\nu_1(S_3^-)$ band compared to green-laser spectra and enhanced Raman signal at this laser wavelength (Supplementary Fig. S2). These Raman features strongly suggest the presence of polysulfide ions (ν_s, cm^{-1}: S_2^- ~590, S_2^{2-} ~451, S_3^{2-} ~476, S_4^- ~384 and 439, S_4^{2-} ~482, S_5^{2-} ~432, S_6^{2-} ~373 and 453; Chivers and Lau, 1982). Polysulfide ions (S_n^{2-}) are known to promote S_3^- formation through their dissociation/disproportionation (Chivers and Elder, 2013). Zero-valent sulfur polymeric molecules, S_n^0, other than $S_8^0{}_{(aq)}$ may also display similar Raman characteristics (ν_s, cm^{-1}: S_2^0 ~717, S_3^0 ~583, S_4^0 ~352 and 674; Chivers and Lau, 1982). S_n^0 species were also detected by Pokrovski and Dubessy (2015) in $K_2S_2O_3$ ± HCl solutions at T above 200°C. However, we believe that S_4^{2-} or S_6^{2-} ions are the major species accounting for the 400-440 cm^{-1} Raman bands because these polysulfides absorb light at 440-450 nm and therefore have a pronounced Raman resonance of their S-S stretching bands with 488 nm laser excitation (Chivers and Lau, 1982). The characteristic H-S Raman vibrations at 2400-2600 cm^{-1} of HS_n^- or $H_2S_n^0$ species (Dubessy et al., 2008) are not detected in our fluid inclusions. The existence of HS_n^- ions in our fluid inclusions at elevated temperatures cannot be excluded; however we have neither clear spectroscopic evidence nor any thermodynamic data to support their presence. Indeed, the stability constants of HS_n^- ions are available only at 25°C (Boulègue and Michard, 1978; Millero, 1986; Williamson and Rimstidt, 1992). At 25°C, the maximum concentration of HS_n^- ions is reached at pH ~ 7, but it remains 3 orders of magnitudes lower than that of S_n^{2-} ions. Polysulfides concentrations decrease under acidic conditions.

Heating-cooling cycles were performed in order to ensure that the formation of S_3^- and polymeric S species was reversible (Supplementary Fig. S3). A fluid inclusion was first heated to 300°C, cooled down to 100°C and heated again to 300°C. The appearance and disappearance of S_3^- and S_n^{2-} ($\pm S_n^0$) species are clearly visible along this temperature path. On re-heating the fluid inclusion to 300°C (i.e. after cooling), one can observe that the Raman peak area ratio of these species is exactly the same than the one recorded previously at the same temperature (Supplementary Fig. S3). Because the aqueous sulfur speciation is dominated by sulfate and sulfide in our fluid inclusions (see below), the reversible formation of S_3^- and S_n^{2-} ($\pm S_n^0$) does not affect significantly the concentration of sulfate and sulfide. In addition, the Raman spectra acquired at T up to 300°C show no changes over 2 hours at a constant temperature. The rapid (few tens of minutes) establishment of a steady state concentration of S_3^- and polymeric S species, and their reversible formation indicate that chemical equilibrium is likely to be attained for these intermediate valence sulfur species.

4.3. Sulfur species concentration in fluid inclusions

The calibration coefficients established above enable estimation of SO_4^{2-}, H_2S and S_3^- concentration from normalized integrated area of their Raman bands in the fluid inclusions (Eq. 1). These concentrations are then converted in molality using Equation 2. The fluid density needed to convert molarity to molality is estimated to be about 1.19 g/cm^3 at 25°C. This estimation is based on the salinities of the fluid inclusion with the assumption that NaCl is the principal constituent in the system (Haas, 1976; Pitzer et al., 1984). Fluid density evolution with T was further calculated using the model provided by Mao and Duan (2008).

The mean total dissolved sulfur concentration (S_{tot}) is 0.14 ± 0.03 mol/kg$_{H2O}$ (i.e. 0.45 wt%) at 25°C, with sulfate and sulfide contributing to 67 ± 2 % and 33 ± 2 % of S_{tot}, respectively in all

inclusions. Upon heating above 100°C, both sulfate and sulfide concentrations increase due to elemental sulfur disproportionation. From 200 to 300°C, S_{tot} concentration remain constant around 0.25 ± 0.13 mol/kg_{H2O} (~0.8 wt%), with sulfate and sulfide being the predominant dissolved sulfur species, and contributing to 41 ± 9 % and 59 ± 9 % of S_{tot} respectively. This change in the sulfate/sulfide ratio from 25°C to 200°C is in line with elemental sulfur disproportionation, which produces 3 times more sulfide than sulfate (Equation 5). The temperature behavior of sulfate and sulfide is identical within errors in all studied fluid inclusions. The established calibration coefficients for S_3^- allow the calculation of its concentrations from 200 to 300°C and reasonable extrapolation down to 150°C. S_3^- accounts for 0.2 to 3 % of S_{tot} in this T range with corresponding mean concentrations increasing from (4.7 ± 2.1) $\times 10^{-4}$ to (7.3 ± 5.6) $\times 10^{-3}$ mol/kg_{H2O} (Fig. 7, Table 1). The maximum measured concentration of S_3^- is 2.9×10^{-2} mol/kg_{H2O} (2780 ppm) at 300°C.

Polymeric S species, other than S_3^-, are more difficult to quantify because of the absence of standards and important discrepancies associated to mass balance calculations, but a rough estimation can be deduced using some assumptions on the calibration coefficients values. We apply either the calibration coefficient of a resonant species (k_{S3-}) or the mean value of the non-resonant sulfur species (estimated by extrapolation of the k_{H2S} and the k_{SO4}) to the normalized area of the main peaks of S_n^{2-} ($\pm S_n^0$) species at 407 cm^{-1}, according to Equation 1. These two calibration coefficients (Supplementary Fig. S5) provide two extreme boundaries for the S_n^{2-} ($\pm S_n^0$) concentration: the upper one is given by the non-resonant calibration coefficients and the lower one is given by S_3^- calibration coefficients. This approach provides a wide range of S_n^{2-} ($\pm S_n^0$) species concentrations covering two orders of magnitude from 2.2×10^{-3} to 1.2×10^{-1}

365 mol/kg_{H2O} at 300°C (Fig. 7). Despite important uncertainty, it is noteworthy that the
366 concentration of the polymeric species is far from being negligible.

367 **5. Discussion**

368 *5.1. Representativeness and preservation of the fluid inclusions*

369 Here, all the studied fluid inclusions display the same textural and chemical features
370 irrespective of their host minerals: i) same irregular shape, ii) same liquid-vapor ratio (≈8% ±
371 4%) and chemistry, iii) same salinities, and iv) same sulfur speciation. The fluid inclusions
372 contain H_2 and CH_4, demonstrating that the reducing conditions have been preserved. This
373 observation does not contradict with the presence of sulfate in the geological fluid because its
374 reduction is under strong kinetic control, and because it is constantly supplied by sulfate minerals
375 dissolution, most notably anhydrite. These characteristics together with the absence of secondary
376 inclusion halo provide strong evidences for very limited post-entrapment modifications (Bodnar,
377 2003). The relatively large range of T_h contrasts with the narrow range of measured salinities. It
378 may indicate different entrapment temperature of a single fluid type during the retrograde
379 metamorphism phase with the lowest T as the limit of fluid entrapment and the highest one the
380 peak of metamorphism conditions around 350°C (Strzersynski et al., 2012). We therefore assume
381 that we analyzed the fluid composition trapped during the exhumation of the evaporites in a
382 closed system (no fluid mixing, and degassing). H_2S migration from deeper reservoirs is highly
383 improbable in the present case, because the fluid inclusions located in the white quartzite from
384 the lower Trias, which is stratigraphically below the carnian evaporites (Strzerzynski et al.,
385 2012), are free of H_2S (Supplementary Table S2).

386 Sulfur speciation investigated here at T above 100°C after few hours of equilibration time is
387 probably far from sulfate-sulfide equilibrium for the two following reasons: i) the reducing

conditions imposed by the presence of both H_2 and CH_4 in the fluid inclusions imply that H_2S is the thermodynamically predicted stable sulfur redox end member, and that the TSR process was not completed, and ii) more than 10 years are required to attain 90% of equilibrium between sulfate and sulfide in aqueous solution at 200°C, neutral pH condition and $\Sigma S = 0.1$ mole/kg_{H2O} (Ohmoto and Lasaga, 1982). By contrast, a local equilibrium between $S\text{-}S_n^0\text{-}S_3^-$ and the dominant sulfate and sulfide forms may be achieved rapidly (within minutes) as demonstrated here by the reversible formation (Supplementary Fig. S3) and the steady state concentration of these sulfur species at T > 200°C in our fluid inclusion. In addition, it has been experimentally demonstrated that S_3^- is formed upon heating sulfate–sulfide mixtures at T ≥ 100°C within few tens of minutes (Truche et al., 2014), without any elemental sulfur or thiosulfate in the system initially. The same conclusion has been reached by Pokrovski and Dubessy (2015) at T ≥ 300°C. In this study, S_3^- has been also observed in some natural fluid inclusions containing only sulfates and sulfides at room temperature and no elemental sulfur (Supplementary Table S1). These independent observations imply that the initial disproportionation of elemental sulfur or thiosulfate is not mandatory for S_3^- and polysulfides to appear and, more importantly, that sulfate cannot be considered as a non-reactive species at the time scale of these experiments, even at temperatures as low as 100°C. Thus, these stable intermediate valence sulfur species will form and remain in solution as long as sulfate and sulfide coexist, and their concentrations can be predicted by thermodynamic modeling (see section 5.2. below).

5.2. Thermodynamic calculations

Equilibrium concentrations of sulfur species in the fluid phase were modeled using the Phreeqc software (Parkhurst and Appelo, 1999) and an updated version of the llnl database (Johnson et al., 1992). The stability constants for S_3^-, S_8^0 and S_n^{2-} were updated using the HKF

411 equation of state and HKF parameters estimated for these species (Johnson et al., 1992;
412 Kamyshny et al., 2007; Pokrovski and Dubessy, 2015 and updated databases at
413 http://geopig.asu.edu/?q=tools; specific details in the Supplementary materials). In the first round
414 of modeling (Fig. 8a), sulfate-sulfide concentrations correspond to our Raman measurements at
415 room temperature (0.09 mol/kg_{H2O} and 0.05 mol/kg_{H2O}, respectively), and the initial amount of
416 elemental sulfur in the system (0.11 mole S) is proportional to the one calculated in the fluid
417 inclusions based on geometrical considerations. The redox potential is imposed by the sulfate-
418 sulfide coexistence. The fluid acidity is buffered by fluid equilibrium with calcite and 10 bars of
419 $P(CO_2)$ that imposed a pH around 5 at T >100°C. Such a pH value is in agreement with the
420 speciation of sulfate (only SO_4^{2-}), sulfide (H_2S and minor HS^-) and carbonate (CO_2 and minor
421 HCO_3^-) observed in the fluid inclusions at elevated T (Supplementary Fig. S8). We advise the
422 reader that this pH value is close to neutrality at T >100°C, because of the strong decrease of the
423 dissociation constant of water (the neutrality decrease from pH = 6 to pH = 5.5 with temperature
424 increasing from 100 to 250°C). This range of pH is compatible with the very low HSO_4^-
425 concentration observed in natural sedimentary formation waters (a typical range of pH is
426 between 6.5 and 8.5 at 25°C; Collins, 1975). The salinity is fixed at 3.3 mol/kg_{H2O} NaCl and 1.6
427 mol/kg_{H2O} $CaCl_2$ to mimic the salinity of our fluid inclusions. The extended Debye-Huckel
428 equation for activity coefficients of NaCl- and $CaCl_2$-dominated electrolytes can be applied to
429 such high ionic strengths with reasonable accuracy in the range of temperature explored in this
430 study (Helgeson et al., 1981). Simulations performed at lower ionic strength (i.e. 1 mol/kg_{H2O})
431 provide very similar results. Over the entire T range (25-300°C) the dominant species are
432 sulfates and sulfides. At T > 100°C, S_3^- is the third most abundant sulfur species predicted in the
433 system with concentrations rising up to 1.37×10^{-3} mol/kg_{H2O} at 200-300°C. These

434 thermodynamic predictions are in perfect agreement with our quantitative measurements using
435 *in-situ* Raman spectroscopy (Table 1 and S10). Concerning other polymeric sulfur species, our
436 preliminary Raman estimations, based on Raman calibration coefficients assumption, give S_n^{2-}
437 ($\pm S_n^0$) concentrations (10^{-3} – 10^{-2} m, Fig. 7) far above those predicted thermodynamically (10^{-5} –
438 10^{-4} m, Fig. 8) and much higher than that of $S_{8(aq)}$. Such conclusions imply that S_n^{2-} and S_n^0
439 species must not be ignored in natural fluids and that further studies are needed to determine
440 properly their thermodynamic stability at high T-P.

441 In a second round of modeling (Fig. 8b, c, d), S_{tot} was fixed at a given value without any
442 specification on the sulfate-sulfide concentrations (elemental sulfur solubility providing the
443 upper limit for S_{tot} concentration in Fig. 8b). The sulfur speciation was then modeled as a
444 function of three different physical-chemical parameters (S_{tot}, $f(O_2)$ and pH). The choice of $f(O_2)$
445 value buffered by Hematite-Magnetite (HM) equilibrium is in line with expectation from typical
446 hydrocarbon reservoirs in nature (Seewald, 2001; Richard et al., 2005). Note that Hematite-
447 Magnetite-Pyrite assemblage, also relevant in the context of deep sedimentary settings gives the
448 same $f(O_2)$ as the HM assemblage, but also control the $f(H_2S)$. In our case, the $f(H_2S)$ is not
449 buffered, because iron is clearly limiting.

450 Whatever the chosen conditions in the sedimentary studied domain, sulfate and sulfide are
451 always the dominant S species. However, S_3^- may represent a significant contribution to the
452 sulfur budget if the following conditions are satisfied: 1) total sulfur concentration above 0.1 m,
453 2) T > 150°C, 3) redox potential or $f(O_2)$ enabling sulfate-sulfide coexistence, i.e. close to the
454 hematite-magnetite buffer, and 4) slightly acidic to neutral pH. Such a conclusion has also been
455 reached for temperatures higher than 200°C by Pokrovski and Dubessy (2015). Figure 8c and d
456 show that when concentration of sulfates is much higher than that of sulfides, S_3^- and other

intermediate valence sulfur species have concentrations lower than 10^{-6} mol/kg_{H2O}. The same scenario is observed, albeit less pronounced, when sulfides concentration is much higher than that of sulfates. However, in this latter case, S_3^- concentration is one or two order of magnitude higher than those of the other intermediate valence sulfur species.

Note that S_n^{2-} and S_n^0 species probably contribute to the sulfur budget in a similar, or even more important, proportion as S_3^- in the range 100-300°C, but their thermodynamic properties are currently poorly constrained at elevated T or unknown and require further studies.

5.3. Geochemical implications

The characteristic blue color of the S_3^- chromophore ion and its UV-visible and Raman spectral patterns in aqueous solutions has already been noticed in numerous experimental studies involving sulfate and sulfide mixtures at T above 100°C (Giggenbach, 1968; Uyama et al., 1985; Pokrovski and Dubrovinsky, 2011; Jacquemet et al., 2014). However, the discovery of both S_3^- and other polymeric S species at the millimolar concentration level at T as low as 100°C in natural fluid inclusions associated with a sedimentary formation where TSR occurred is a new finding. These new data from natural samples corroborate the experimental discovery that S_3^- is a major stable intermediate valence S species involved in the reaction path of abiogenic sulfate reduction (Truche et al., 2014), and support the fact that disproportionation reaction of sulfur is a key step for TSR (Yuan et al., 2013). The onset temperature of TSR in nature around 100–140°C corresponds remarkably well to the rise of S_3^- and S_n^0 concentrations (Fig. 7 and Fig. 8a). Therefore, S_3^- is an important reactive species in the TSR process for the following reasons: i) the radical nature makes it very reactive, ii) the high concentration compared to the other potential intermediate valence sulfur species taking part in the TSR process increases the contact probability with the reducing agent, and iii) the TSR process itself results from an interaction

480 between S_3^- and the electron donor that shift the equilibrium between sulfate and sulfide (Truche
481 et al., 2014).

482 This study opens up new perspectives on TSR isotopic record (Watanabe et al., 2009; Oduro
483 et al., 2011; Gvirtzman et al., 2015; Cai et al., 2016; Meshoulam et al., 2016). Indeed, there are
484 numerous similarities between the reaction mechanisms of sulfate-sulfide isotope exchange and
485 the multistep change in oxidative state of sulfur during the TSR process (Ohmoto and Lasaga,
486 1982; Goldstein and Aizenshtat, 1994). The kinetics of both reactions are strongly dependent
487 upon temperature, pH and sulfate-sulfide concentrations, because these parameters play a
488 primary role on the speciation and concentration of the intermediate valence sulfur species,
489 which act as a bridge for electron transfer between sulfate and sulfide. We suggest that the rapid
490 formation of S_3^-, S_n^{2-} and S_n^0 species is a stage allowing TSR and sulfur isotope exchange to
491 occur, and not thiosulfate, or polythionates as believed previously (e.g., Ohmoto and Lasaga,
492 1982). The rapid decrease of S_3^- and S_n^{2-} concentration at pH above 6 at 200°C (Fig. 8d; Chu et
493 al., 2004) reflect well the decrease of the reaction rate of sulfate-sulfide isotope exchange and
494 TSR under alkaline condition. Under strongly acidic condition, it is probable that S_n^0 together
495 with sulfate speciation (dominated by HSO_4^- a non-symmetric, so more reactive species) and the
496 abundance of proton (TSR imply a net consumption of H^+, see Equation 4) explain the increase
497 of the TSR reaction rate (Truche et al., 2009; Pokrovski and Dubessy, 2015). These intermediate
498 valence sulfur species may also facilitate electron transfer between carbon species and enhance
499 the rates of reaction between hydrocarbons, methane and CO_2 (Seewald, 2003).

500 Despite its complexity, TSR is a common reaction in numerous geological settings and
501 represents a key geochemical process in many environments where mass transfer and chemical
502 fractionation are involved. The high concentrations of these intermediate valence S species at T

503 >100°C place significant constraints on the formation of sour gas fields (Machel, 2001; Cai et
504 al., 2003) and sulfide ore deposits (e.g. Mississippi Valley-type deposits, Volcanogenic-Massive
505 Sulfide deposits) where reduced sulfur originates from TSR (Huston et al., 2001; Thom and
506 Anderson, 2008). In geologic conditions, bacterial sulfate reduction at the earliest stage of
507 diagenesis, or the thermal decomposition of sulfur bearing organic compounds, or fluid mixing
508 with sulfide-rich solution, or elemental sulfur disproportionation may provide the necessary
509 reduced sulfur to initiate TSR at T >100°C (Fig. 9; Machel, 2001). The TSR process itself may
510 occur under physico-chemical conditions that enhance the stability and concentration of S_3^- and
511 S_n^{-2} ($\pm S_n^0$) species: high sulfate-sulfide concentration, T >100°C, and circum-neutral pH
512 conditions. The direct effect of S_3^- and polymeric S species on base metal solubility (e.g. Pb, Zn,
513 Cu) were only broadly estimated by Pokrovski et al. (2015) but remains to be more evaluated.
514 The presence of non-negligible concentrations of S_3^- and polymeric species in deep
515 sedimentary brines may also have important consequence for petroleum alteration and
516 organosulfur compounds (OSCs) formation during the TSR process (Seewald, 2001 and 2003;
517 Amrani, 2014). There is currently a significant research effort to document the effect of TSR on
518 non-volatile high molecular weight aromatic and polar organic species (e.g. Walters et al., 2015;
519 Meshoulam et al., 2016). It has been suggested that H_2S reacts with hydrocarbons to form OSCs
520 (e.g., thiols, sulfides, thiophenes, and condensed thiophenes) that in turn catalyze TSR (Amrani
521 et al., 2008; Zhang et al., 2008). Intermediate oxidation-state S species such as elemental S,
522 polysulfides, sulfites or thiosulfates have been also proposed as possible sources for OSCs
523 formation during TSR (Goldstein and Aizenshtat, 1994; Lewan, 1998). However, elemental S
524 and thiosulfates are poor nucleophiles and break down into sulfate and sulfide at T >100°C,
525 which make them unfavorable candidate for the reaction with organic matter under deep

sedimentary conditions. By contrast, the strong nucleophile character of polysulfides and the S_3^- ion (Chivers and Elder, 2013), suggests that these species are more prone to react with hydrocarbons than H_2S or elemental S. Sulfur isotope fractionation associated with the formation of OSCs is a potential tracer for the occurrence and extent of TSR (Amrani, 2014; Gvirtzman et al., 2015; Cai et al., 2016; Meshoulam et al., 2016). However, important mechanistic details about the overall TSR process are still missing and prevent full explanation of the sulfur isotope records. We suggest that polymeric sulfur species and, in particular, the S_3^- ions should be considered in the sulfur isotopic fractionation model to bring back together laboratory and field observations.

6. Conclusions and perspectives

The main conclusions from this study are:

1. We reveal for the first time the formation of the trisulfur S_3^- ion and other polymeric S species (S_n^{2-} $\pm S_n^0$) at T >100°C in natural fluids from typical deeply buried sedimentary environment where TSR occurred.
2. The concentration of S_3^- ion can reach 2800 ppm at 300°C in fluid inclusions containing sulfate-sulfide concentration above 0.1 mol/kg_{H2O}.
3. This work confirms the previous findings that S_3^- is a major stable intermediate valence S species involved in the reaction path of TSR. The onset temperature of TSR in nature around 100–140°C corresponds remarkably well to the rise of S_3^- and other polymeric S species concentrations in the fluid inclusions.
4. The TSR process itself occurs under physico-chemical conditions that enhance the stability and concentration of S_3^- and S_n^{2-} ($\pm S_n^0$) species: high sulfate-sulfide concentration, T ≥100°C, and circum-neutral pH conditions.

5. This study opens up new perspectives on TSR isotopic record and into the S-chain radical reactions involved in organic-inorganic interactions, where sulfur speciation play a key role.

The discovery of the trisulfur S_3^- ion and other polymeric S species, in natural geological fluid at T ≥100°C, may also encourage new investigations on sulfur speciation in natural geological fluids associated with metamorphism, mid-oceanic ridge hydrothermal fluid circulation and magmatic/porphyry settings where sulfate and sulfide often coexist.

Acknowledgements

This work was funded by LABEX ANR-10-LABX-21-01 Ressources21 (Strategic metal resources of the 21st Century) and the French Ministry of Higher Education and Research. The authors are extremely grateful to M.C. Jodin-Caumon and P. Robert for technical assistance during Raman spectroscopic analysis and O. Barrès during Infrared spectroscopic analysis. The paper benefited greatly from the review provided by G. Pokrovski, H. Ohmoto and one anonymous reviewer. We thank M. Böttcher for editorial support.

References

Amrani, A., Zhang, T., Ma, Q., Ellis, G.S., Tang, Y., 2008. The role of labile Sulphur compounds in thermal sulphate reduction. Geochim. Cosmochim. Acta 72, 2960–2972.

Amrani, A., 2014. Organosulfur compounds: molecular and isotopic evolution from biota to oil and gas. Annu. Rev. Earth Planet. Sci. 42, 733-768.

Barnes, H.L., 1997. Geochemistry of Hydrothermal Ore Deposits, Wiley, New York.

Basuki, N.I., Taylor, B.E., Spooner, E.T.C., 2008. Sulfur isotope evidence for thermochemical reduction of dissolved sulfate in Mississippi Valley-Type zinc-lead mineralization, Bongara Area, Northern Peru. Econ. Geol. 103, 783-799.

572 Bodnar, R.J., 2003. Reequilibration of fluid inclusions: Fluid inclusions: Analysis and
573 interpretation. *In* Samson, I., Anderson, A., and Marshall, D., eds, Mineralogical Association
574 of Canada, Short Course 32, 213-230.
575 Bodnar, R.J., Bethke, P.M., 1984. Systematics of stretching of fluid inclusions I: Fluorite and
576 sphalerite at 1 atmosphere confining pressure. Econ. Geol. 79, 141-161.
577 Boiron, M-C., Moissette, A., Cathelineau, M., Banks, D., Monnin, C., and Dubessy, J., 1999.
578 Detailed determination of palaeofluid chemistry: an integrated study of sulphate-volatile rich
579 brines and aquo-carbonic fluids in quartz veins from Ouro Fino (Brazil). Chem. Geol. 154,
580 179-192.
581 Boulègue, J., 1978. Metastable sulfur species and trace metals (Mn, Fe, Cu, Zn, Cd, Pb) in hot
582 brines from the French Dogger. Am. J. Sci. 278, 1394–1411.
583 Boulègue, J., Michard, G., 1978. Constantes de formation des ions polysulfurés S_6^{2-}, S_5^{2-} et S_4^{2-}
584 en phase aqueuse. J. Fr. Hydrologie 9, 27-34 (in french).
585 Cai, C., Amrani, A., Worden, R.H., Xiao, Q., Wang, T., Gvirtzman, Z., Li, H., Said-Ahmad, W.,
586 Jia, L., 2016. Sulfur isotopic compositions of individual organosulfur compounds and their
587 genetic links in the Lower Paleozoic petroleum pools of the Tarim Basin, NW China.
588 Geochim. Cosmochim. Acta 182, 88-108.
589 Cai, C., Worden, R.H., Bottrell, S.H., Wang, L., Yang, C., 2003. Thermochemical sulphate
590 reduction and the generation of hydrogen sulphide and thiols (mercaptans) in Triassic
591 carbonate reservoirs from the Sichuan Basin, China. Chem. Geol. 202, 39-57.
592 Caumon, M.C, Dubessy, J., Robert, P., Tarantola, A., 2013. Fused-silica capillary capsules
593 (FSCCs) as reference synthetic aqueous fluid inclusions to determine chlorinity by Raman
594 spectroscopy. Eur. J. Mineral. 25, 755-763.

595 Chivers, T., Elder, P.J.W., 2013. Ubiquitous trisulfur radical anion: fundamentals and
596 applications in materials science, electrochemistry, analytical chemistry and geochemistry.
597 Chem. Soc. Rev. 42, 5996-6005.
598 Chivers, T., Lau, C., 1982. Raman spectroscopic identification of the S_4N^- and S_3^- ions in blue
599 solutions of sulfur in liquid ammonia. Inorg. Chem. 21, 453-455.
600 Chou, I-M., Song, Y., Burruss, R.C., 2008. A new method for synthesizing fluid inclusions in
601 fused silica capillaries containing organic and inorganic material. Geochim. Cosmochim.
602 Acta 72, 5217-5231.
603 Chu, X., Ohmoto, H., Cole, D.R., 2004. Kinetics of sulfur isotope exchange between aqueous
604 sulfide and thiosulfate involving intra- and intermolecular reactions at hydrothermal
605 conditions. Chem. Geol. 211, 217-235.
606 Collins, A.G., 1975. Geochemistry of oilfield waters. Elsevier, Amsterdam, The Netherlands,
607 496 p.
608 Cross, M.M., Manning, D.A.C., Bottrell, S.H., Worden, R.H., 2004. Thermochemical sulphate
609 reduction (TSR): experimental determination of reactions kinetics and implications of the
610 observed reaction rates for petroleum reservoirs. Org. Geochem. 35, 393-404.
611 Debelmas, J., Desmons, J., Ellenberger, F., Goffé, B., Fabre, J., Jaillard, E., and Pachoud, A.,
612 1989a. Notice explicative de la feuille Modane. B.R.G.M., scale 1/50 000, 1 sheet, 53 p. text
613 (in french).
614 Debelmas, J., Desmons, J., Ellenberger, F., Goffé, B., Fabre, J., 1989b. Carte géologique de la
615 France, feuille de Modane. B.R.G.M., scale 1/50000.

Dubessy, J., Audeoud, D., Wilkins, R., Kosztolanyi, C., 1982. The use of the Raman microprobe mole in the determination of the electrolytes dissolved in the aqueous phase of fluid inclusions. Chem. Geol. 37, 137-150.

Dubessy, J., Leisen, J.P., Lhomme, T., Pironon, J., 2008. Measurements of concentration ratios of polysulfanes in mixtures solvent-sulfur-sulfanes. Unpublished rapport (in French).

Dubessy, J., Lhomme, T., Boiron, M-C., Rull, F., 2002. Determination of chlorinity in aqueous fluids using Raman spectroscopy of the stretching band of water at room temperature: Application to fluid inclusions. Appl. Spectrosc. 56, 99-106.

Gabalda, S., Beyssac, O., Jolivet, L., Agard, P., Chopin, C., 2009. Thermal structure of a fossil subduction wedge in the Western Alps. Terra Nova 21, 28-34.

Giggenbach, W., 1968. On the nature of the blue solutions of sulfur. J. Inorg. Nucl. Chem. 30, 3189-3201.

Giggenbach, W.F., 1974. Equilibrium involving polysulphide ions in aqueous sulphide solutions up to 240°C. Inorg. Chem. 13, 1724–1730.

Goldhaber, M.B., Orr, W.L., 1995. Kinetic controls on thermochemical sulphate reduction as a source of sedimentary H_2S. In: Vairavamurthy, M.A., Schoonen, M.A.A. (Eds.), Geochemical Transformations of Sedimentary Sulphur. American Chemical Society.

Goldstein, T.P., Aizenshtat, Z., 1994. Thermochemical sulfate reduction: A review. J. Therm. Anal. 42, 241-290.

Gvirtzman, Z., Said-Ahmad, W., Ellis, G.S., Hill, R.J., Moldowan, J.M., Wei, Z., Amrani, A., 2015. Compound-specific sulfur isotope analysis of thiadiamondoids of oils from the Smackover Formation, USA. Geochim. Cosmochim. Acta 167, 144-161.

638 Haas, J.L., 1976. Physical properties of the coexisting phases and thermochemical properties of
639 the H2O component in boiling NaCl solutions. U.S.G.S. Bulletin 1421-A, 73 p.
640 Helgeson, H.C., Kirkham, D.H., Flowers, G.C., 1981. Theoretical prediction of the
641 thermodynamic behavior of aqueous electolytes at high pressures and temperatures: IV.
642 Calculation of activity coefficients, osmotic coefficients, and apparent molal and standard
643 and relative partial molal properties to 600°C and 5kb. Am. J. Sci. 281, 1249-1516.
644 Heydari, E., Moore, C.H., 1989. Burial diagenesis and thermochemical sulfate reduction,
645 Smackover Formation, southeastern Mississippi salt basin. Geology, 17, 1080-1084.
646 Horita, J., Zimmermann, H., Holland, H.D., 2002. Chemical evolution of seawater during the
647 Phanerozoic: Implications from the record of marine evaporites. Geochim. Cosmochim.
648 Acta 66, 3733-3756.
649 Huston, D.L., Brauhart, C.W., Drieberg, S.L., Davidson, G.J., Groves, D.I., 2001. Metal leaching
650 and inorganic sulfate reduction in volcanic-hosted massive sulfide minerals systems:
651 Evidence from the paleo-Archean Panorama district, Western Australia. Geology 29, 687-
652 690.
653 Jacquemet, N., Guillaume, D., Zwick, A., Pokrovski, G.S., 2014. In situ Raman spectroscopy
654 identification of the S_3^- ion in S-rich hydrothermal fluids from synthetic fluid inclusions.
655 Am. Mineral. 99, 1109-1118.
656 Johnson, J.W., Oelkers, E.H., Helgeson, H.C., 1992. SUPCRT92: A software package for
657 calculating the standard molal thermodynamic properties of minerals, gases, aqueous
658 species, and reactions from 1 to 5000 bar and to 0 to 1000°C. Comput. Geosci. 18, 899-947.
659 Kaasalainen, H., Stefánsson, A., 2011. Sulfur speciation in natural hydrothermal waters, Iceland.
660 Geochim. Cosmochim. Acta 75, 2777-2791.

661 Kamyshny, A., Jr., Gun, J., Rizkov, D., Voitsekovski, T., Lev, O., 2007. Equilibrium distribution
662 of polysulfide ions in aqueous solutions at different temperatures by rapid single phase
663 derivatization. Environ. Sci. Technol. 41, 2395-2400.
664 Kamyshny, A., Jr., Zilberbrand, M., Ekeltchik, I., Voitsekovski, T., Gun, J., Lev, O., 2008.
665 Speciation of polysulfides and zerovalent sulfur in sulfide-rich water wells in Southern and
666 Central Israel. Aquat. Geochem. 14, 171-192.
667 Kiyosu, Y., Krouse, H.R., 1993. Thermochemical reduction and sulphur isotopic behavior of
668 sulfate by acetic-acid in the presence of native sulphur. Geochem. J. 27, 49.
669 Lanari, P., Guillot, S., Schwartz, S., Vidal, O., Tricart, P., Riel, N., Beyssac, O., 2012.
670 Diachronous evolution of the alpine continental subduction wedge: evidence from P–T
671 estimates in the Brianc¸ onnais Zone houillère (France – Western Alps). J. Geodyn. 56-57,
672 39–54.
673 Lewan, M.D., 1998. Sulphur-radical control on petroleum formation rates. Nature 391, 164-166.
674 Ma, Q., Ellis, G.S., Amrani, A., Zhang, T., Tang, Y., 2008. Theoretical study on the reactivity of
675 sulfates species with hydrocarbons. Geochim. Cosmochim. Acta 72, 4565-4576.
676 Machel, H.G., 2001. Bacterial and thermochemical sulfate reduction in diagenetic settings – old
677 and new insights. Sediment. Geol. 140, 143-175.
678 Mao, S., Duan, Z., 2008. The P,V,T,χ properties of binary aqueous chloride solutions up to T =
679 573 K and 100 MPa. J. Chem. Thermodyn. 40, 1046-1063.
680 Mavrogenes, J.A., Bodnar, R.J., 1994. Hydrogen movement into and out of fluid inclusions in
681 quartz: Experimental evidence and geologic implications. Geochim. Cosmochim. Acta 58,
682 141-148.

683 Meshoulam, A., Ellis, G.S., Said Ahmad, W., Deev, A., Sessions, A.L., Tang, Y., Adkins, J.F.,
684 Jinzhong, L., Gilhooly III, W.P., Aizenshtat, Z., Amrani, A., 2016. Study of thermochemical
685 sulfate reduction mechanism using compound specific sulfur isotope analysis. Geochim.
686 Cosmochim. Acta 188, 73-92.
687 Millero, F.J., 1986. The thermodynamics and kinetics of the hydrogen sulfide system in natural
688 waters. Mar. Chem. 18, 121-147.
689 Nordstrom, D.K., McCleskey, R.B., Ball, J.W., 2009. Sulfur geochemistry of hydrothermal
690 waters in Yellowstone National Park: IV Acid-sulfate waters. Appl. Geochem. 24, 191-207.
691 Oduro, H., Harms, B., Sintim, H.O., Kaufman, A.J., Cody, G., Farquhar, J., 2011. Evidence of
692 magnetic isotope effects during thermochemical sulfate reduction. Proc. Natl. Acad. Sci.
693 U.S.A. 108, 17635-17638.
694 Ohmoto, H., Lasaga, A.C., 1982. Kinetics of reactions between aqueous sulfates and sulfides in
695 hydrothermal systems. Geochim. Cosmochim. Acta 46, 1727-1745.
696 Orr, W.L., 1974. Changes in sulfur content and isotopic-ratios of sulfur during petroleum
697 maturation – study of Big Horn Basin Paleozoic oils. AAPG Bulletin 58, 2295-2318.
698 Parkhurst, D.L., Appelo, C.A.J., 1999. User's guide to PHREEQC (version 2)- A computer
699 program for speciation, batch-reaction, one-dimensional transport, and inverse geochemical
700 calculations. U.S.G.S. Water-Res. Invest. Rep. 99-4259, Denver, Colorado, USA, 312 p.
701 Pitzer, K.S., Peiper, J.C., Busey, R.H., 1984. Thermodynamics properties of aqueous sodium
702 chloride solutions. J. Phys. Chem. Ref. Data 13, 1-102.
703 Pokrovski, G.S., Dubessy, J., 2015. Stability and abundance of the trisulfur radical ion S_3^- in
704 hydrothermal fluids. Earth Planet. Sci. Lett. 411, 298-309.

Pokrovski, G.S., Dubrovinsky, L.S., 2011. The S_3^- ion is stable in geological fluids at elevated temperatures and pressures. Science 331, 1052-1054.

Pokrovski, G.S., Kokh, M.A., Guillaume, D., Borisova, A.Y., Gisquet, P., Hazemann, J-L., Lahera, E., Del Net, W., Proux, O., Testemale, D., Haigis, V., Jonchière, R., Seitsonen, A.P., Ferlat, G., Vuilleumier, R., Saitta, A.M., Boiron, M-C., and Dubessy, J., 2015, Sulfur radical species form gold deposits on Earth: Proc. Natl. Acad. Sci. U.S.A., 112, 13484-13489.

Richard L., Neuville N., Sterpenich J., Perfetti E. and Lacharpagne J.C., Thermodynamic analysis of organic/inorganic reactions involving sulfur: implications for the sequestration of H2S in carbonate reservoirs, Oil Gas Sci. Technol., 60, 275-285.

Seewald, J.S., 2001. Aqueous geochemistry of low molecular weight hydrocarbons at elevated temperatures and pressures: Constraints from mineral buffered laboratory experiments. Geochim. Cosmochim. Acta 65, 1641-1664.

Seewald, J.S., 2003. Organic-inorganic interactions in petroleum-producing sedimentary basins. Nature 426, 327-333.

Servoss, R.R., Clark, H.M., 1957. Vibrational spectra of normal and isotopically labeled boric acid. J. Chem. Phys. 26, 1175-1178.

Steele-MacInnis, M., Bodnar, R.J., Naden, J., 2011. Numerical model to determine the composition of H2O-NaCl-CaCl2 fluid inclusions based on microthermometric and microanalytical data. Geochim. Cosmochim. Acta 75, 21-40.

Steudel, R., 2003. Elemental Sulfur and Sulfur-rich Compounds I, II. Springer, Berlin.

Strzerzynski, P., Guillot, S., Leloup, P.H., Arnaud, N., Vidal, O., Ledru, P., Courrioux, G., Darmendrail, X., 2012. Tectono-metamorphic evolution of the Briançonnais zone (Modane-

727 Aussois and Southern Vanoise units, Lyon Turin transect, Western Alps). J. Geodyn. 56-57,
728 55-75.
729 Takano, B., 1987. Correlation of volcanic activity with sulfur oxyanion speciation in a crater
730 lake. Science 235, 1633–1635.
731 Takano, B., Ohsawa, S., Glover, R.B., 1994. Surveillance of Ruapehu Crater, New Zealand, by
732 aqueous polythionates. J. Volcanol. Geotherm. Res. 60, 29–57.
733 Thom, J., Anderson, G.M., 2008. The role of thermochemical sulfate reduction in the origin of
734 Mississippi Valley-Type deposits. I. Experiemental results. Geofluids 8, 16-26.
735 Truche, L., Bazarkina, E.F., Barré, G., Thomassot, E., Berger, G., Dubessy, J., Robert, P., 2014.
736 The role of S_3^- ion in thermochemical sulphate reduction: Geological and geochemical
737 implications. Earth Planet. Sci. Lett. 396, 190-200.
738 Truche, L., Berger, G., Destrigneville, C., Pages, A., Guillaume, D., Giffaut, E., Jacquot, E.,
739 2009. Experimental reduction of aqueous sulphate by hydrogen under hydrothermal
740 conditions: implication for the nuclear waste storage. Geochim. Cosmochim. Acta 73, 4824–
741 4835.
742 Uyama, F., Chiba, H., Kusakabe, M., Sakai, H., 1985. Sulfur isotope exchange reactions in the
743 aqueous system: thiosulfate-sulfide-sulfate at hydrothermal temperature. Geochem. J. 19,
744 301-315.
745 Vanko, D.A., Bach, W., 2005. Heating and freezing experiments on aqueous fluid inclusions in
746 anhydrite: recognition and effects of stretching and the low-temperature formation of
747 gypsum. Chem. Geol. 223, 35-45.
748 Veldeman, E., Van't dac, L., Gijbels, R., Pentcheva, E., 1991. Sulfur species and associated trace
749 elements in south-west Bulgarian thermal waters. Appl. Geochem. 6, 49–62.

Walters, C.C., Wang, F.C., Qian, K., Wu, C., Mennito, A.S., Wei, Z., 2015. Petroleum alteration by thermochemical sulfate reduction – A comprehensive molecular study of aromatic hydrocarbons and polar compounds. Geochim. Cosmochim. Acta 153, 37-71.

Wang, C.H., Wright, R.B., 1973. Effect of density on the Raman scattering of molecular fluids. I. A detailed study of the scattering polarization, intensity, frequency shift, and spectral shape in gaseous N_2. J. Chem. Phys. 59, 1706-1712.

Watanabe, Y., Farquhar, J., Ohmoto, H., 2009. Anomalous fractionations of sulfur isotopes during thermochemical sulfate reduction. Science 324, 370-373.

Webster, J.G., 1987. Thiosulfate in surficial geothermal waters, North Island, New Zealand. Appl. Geochem. 2, 579–584.

Williamson, M.A., Rimstidt, J.D., 1992. Correlation between structure and thermodynamic properties of aqueous sulfur species. Geochim. Cosmochim. Acta 56, 3867-3880.

Worden, R.H., Smalley, P.C., 1996. H_2S-producing reactions in deep carbonate gas reservoirs: Khuff Formation, Abu Dhabi. Chem. Geol. 133, 157-171.

Worden, R.H., Smalley, P.C., Barclay, S.A., 2003. H_2S and diagenetic pyrite in North Sea sandstones: due to TSR or organic sulphur compound cracking?. J. Geochem. Explor. 78-79, 487-491.

Xu, Y., Schoonen, M.A.A., Nordstrom, D.K., Cunningham, K.M., Ball, J.W., 1998. Sulfur geochemistry of hydrothermal waters in Yellowstone National Park, Wyoming, USA: I. Origin of thiosulfate in selected hot spring waters. Geochim. Cosmochim. Acta 62, 3729–3743.

771 Yuan, S., Chou, I-M., Burruss, R.C., Wang, X., Li, J., 2013. Disproportionation and
772 thermochemical sulfate reduction reactions in S-H_2O-CH_4 and S-D_2O-CH_4 systems from
773 200 to 340 °C at elevated pressures. Geochim. Cosmochim. Acta 118, 263-275.
774 Zhang, T., Amrani, A., Ellis, G.S., Ma, Q., Tang, Y., 2008. Experimental investigation on
775 thermochemical sulphate reduction by H_2S initiation. Geochim. Cosmochim. Acta 72, 3518–
776 3530.

777 **Appendix A. Supplementary material**

778 Supplementary information is available in the attached file.

779

780 **TABLE**

781 **Table 1.** Sulfur species concentrations (mol/kg_{H2O}) measured in natural fluid inclusions
782 representative for TSR processes in the Arc Valley (French Alps).

783 **FIGURE CAPTIONS**

784 **Fig. 1.** Simplified geological map of the Arc Valley (France) with the sampling locations
785 (modified from Debelmas et al., 1989b).

786 **Fig. 2.** (a) Typical outcrops of the sampled Carnian evaporite from the Arc Valley (France)
787 showing schistosity in the anhydrite and up to 2 m in diameter dolomitc “boudins”. (b)
788 Uncolored to purple fluorite crystals in association with native sulfur disseminated in anhydrite
789 or located in fractures affecting the cryptocrystalline dolomite. (c) Native sulfur occurrence in
790 association with anhydrite and dolomite. (d) Pyrite associated to anhydrite and crystalline white
791 dolomite. Abbreviations: CcD = cryptocrystalline dolomite; Anh = anhydrite; S = elemental
792 sulfur; Fl = fluorite; WD = white dolomite; Py = pyrite.

Fig. 3. Microthermometry results of fluid inclusions from the Arc Valley (France). (a) Histogram of homogenization temperatures (Th). (b) Histogram of last ice melting temperatures (Tm ice).

Fig. 4. Raman calibration coefficients (k_i) for the 514 nm laser excitation for sulfur species as function of temperature (°C). (a) Calibration coefficients for the major sulfur species as deduced from standard solutions. Note the slight effect of salinity on the calibration coefficients of SO_4^{2-}. (b) Calibration coefficients for S_3^- (k_{S3-}) deduced and used in this study and k_{S3-} from Pokrovski and Dubessy (2015). Calculations are done according to equation 3 assuming the same temperature dependence as for H_2S.

Fig. 5. Raman spectra of the several phases in the fluid inclusions at room temperature. (a) Typical Raman spectrum of the vapor phase of fluid inclusions hosted in fluorite. CO_2 and H_2S are the main component of the gas phase. Raman spectra were acquired using the 514 nm (green) Ar^+ laser excitation. N_2, CH_4 and H_2 are also present. The broad, but weakly intense, O-H stretching band of liquid water between 2800-3700 cm^{-1} is also visible on this Raman spectrum, because the gas bubble moves slightly during the measurements, and the liquid phase may be impacted by the laser beam. (b) Zoom on the 2280-2380 cm^{-1} region and comparison with a Raman spectrum of air (green curve). The splitting of the N_2 band (red curve) demonstrates the presence of N_2 under pressure in the gas phase of the fluid inclusion (see above). (c) Typical Raman spectra of the aqueous phase of fluid inclusions hosted in quartz and fluorite. Note that the composition of fluid inclusions is similar whatever the host mineral. (d) Our measurement allows resolving the contribution of HS^- and H_2S stretching vibration (2570 and 2582 cm^{-1}, respectively) in the Raman peak located at 2400-2700 cm^{-1}. (e), (f) and (g) Raman spectra of the solids phases observed in the fluid inclusions hosted in fluorite and comparison with their

reference in the RRUFF database (http://rruff.info/). Native sulfur spherule is always observed. (e) Anhydrite, (f) calcite and (g) celestine are also observed in few fluid inclusions.

Fig. 6. Raman spectra of the aqueous phase of fluid inclusions hosted in fluorite (a) and quartz (b and c) from the Carnian evaporite (French Alps) recorded at 25 to 300°C. Vertical dashed lines indicate the vibration mode (υ = stretching, δ = bending) and position of major Raman peaks for the respective species in the inclusion. Stars indicate the host mineral peaks.

Fig. 7. Temperature evolution of sulfur speciation in natural fluid inclusions from the Carnian evaporites formation (French Alps). At high temperature, trisulfur radical ion S_3^- (blue circles) and S_n^{2-} $\pm S_n^0$ (estimated in grey shaded area) attain significant concentrations. During cooling, their concentrations drop and only sulfates and sulfides are detected at 25°C.

Fig. 8. Thermodynamic modeling of sulfur speciation as a function of (a) temperature at pH ~ 5 (buffered by fluid equilibrium with calcite and 10 bar CO_2) and redox controlled by sulfate/sulfide equilibrium; (b) total S content at 200°C, pH = 5 and $f(O_2)$ buffered by the hematite-magnetite (HM) assemblage; (c) oxygen fugacity at 200°C and pH = 5; (d) pH at 200°C and $f(O_2)$ of HM. All calculations (lines) are performed for Psat and fluid salinity of 4 m NaCl and 1 m $CaCl_2$. Symbols represent S species concentrations measured in the natural fluid inclusions. PPM = Pyrite–Pyrrhotite–Magnetite and HM = Hematite–Magnetite.

Fig. 9. Conceptual model of TSR and associated processes in deep sedimentary settings highlighting the role of intermediate valence sulfur species.

Figure 1

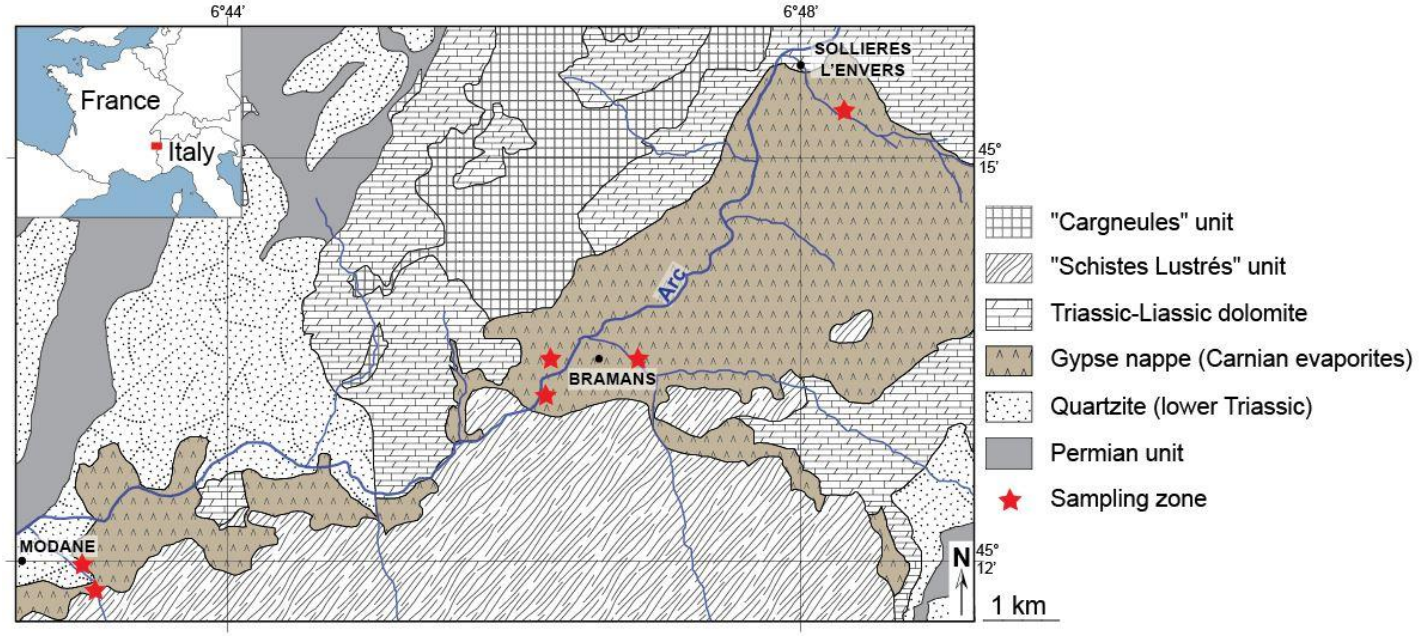
6°44'
6°48'
France
Italy
SOLLIERES
L'ENVERS
45°
15'
Arc
BRAMANS
MODANE
N
45°
12'
1 km
"Cargneules" unit
"Schistes Lustrés" unit
Triassic-Liassic dolomite
Gypse nappe (Carnian evaporites)
Quartzite (lower Triassic)
Permian unit
Sampling zone

838 **Figure 2**

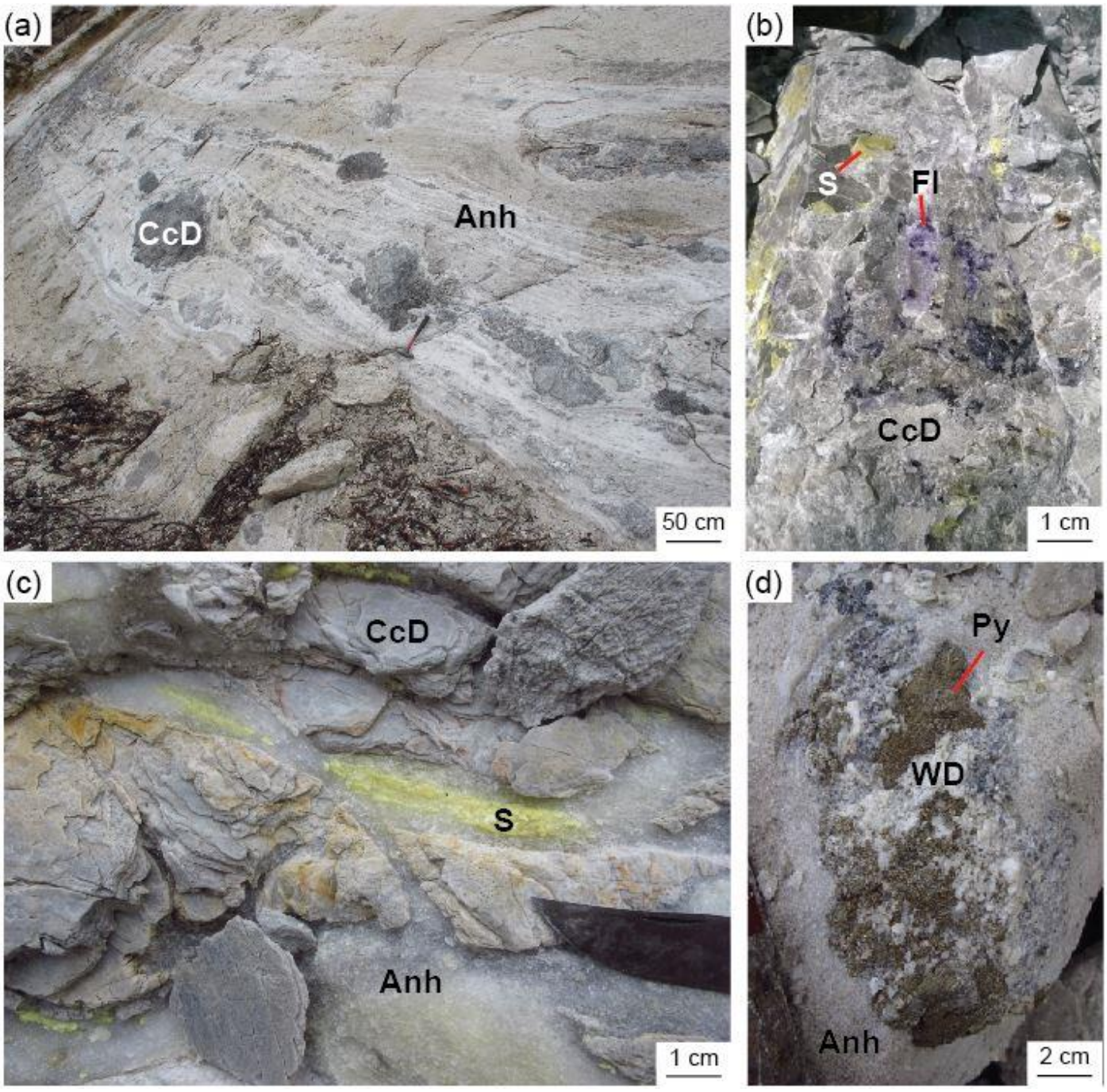

839

840

841 **Figure 3**

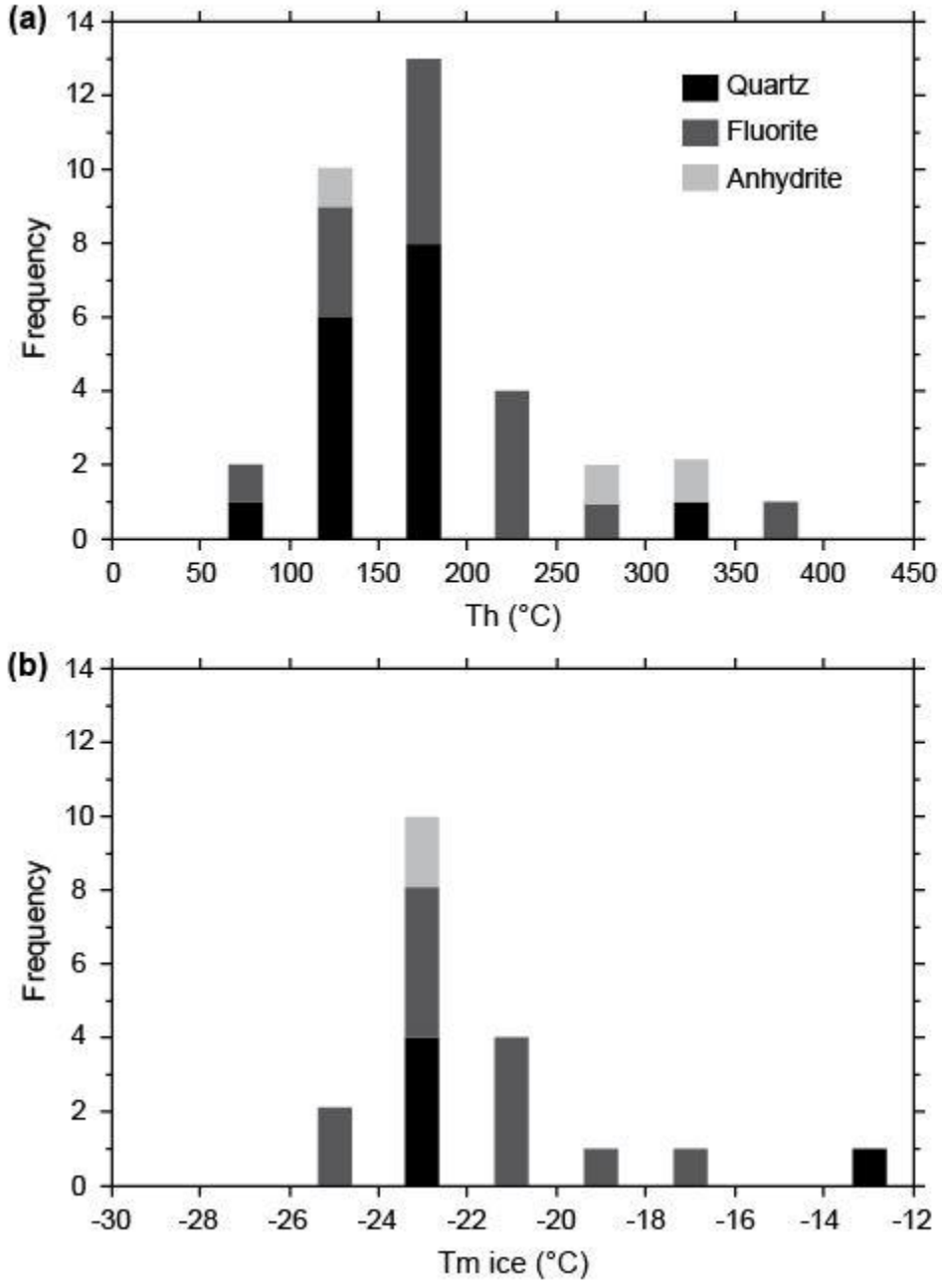

842

843

844 **Figure 4**

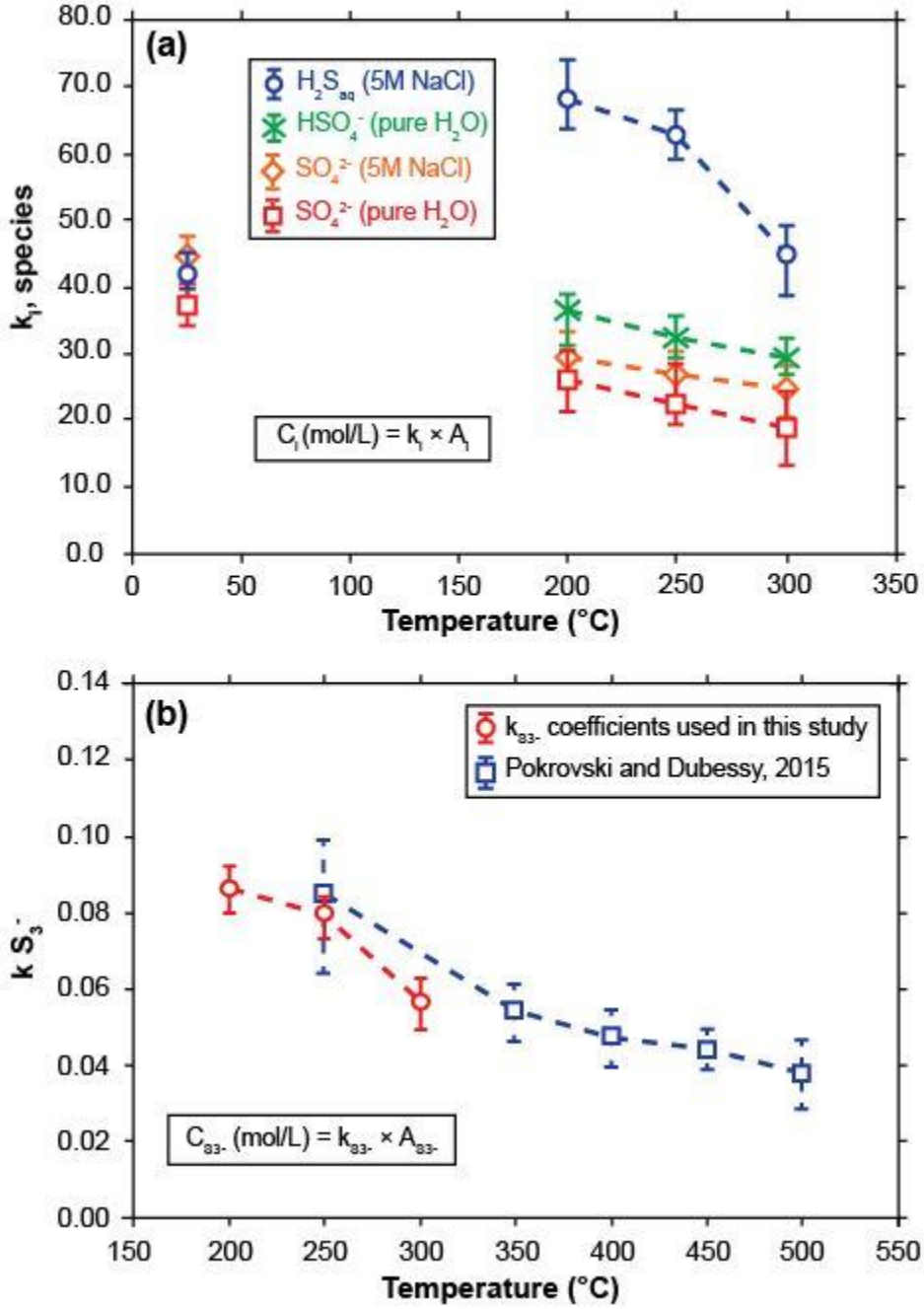

845

846

847 **Figure 5**

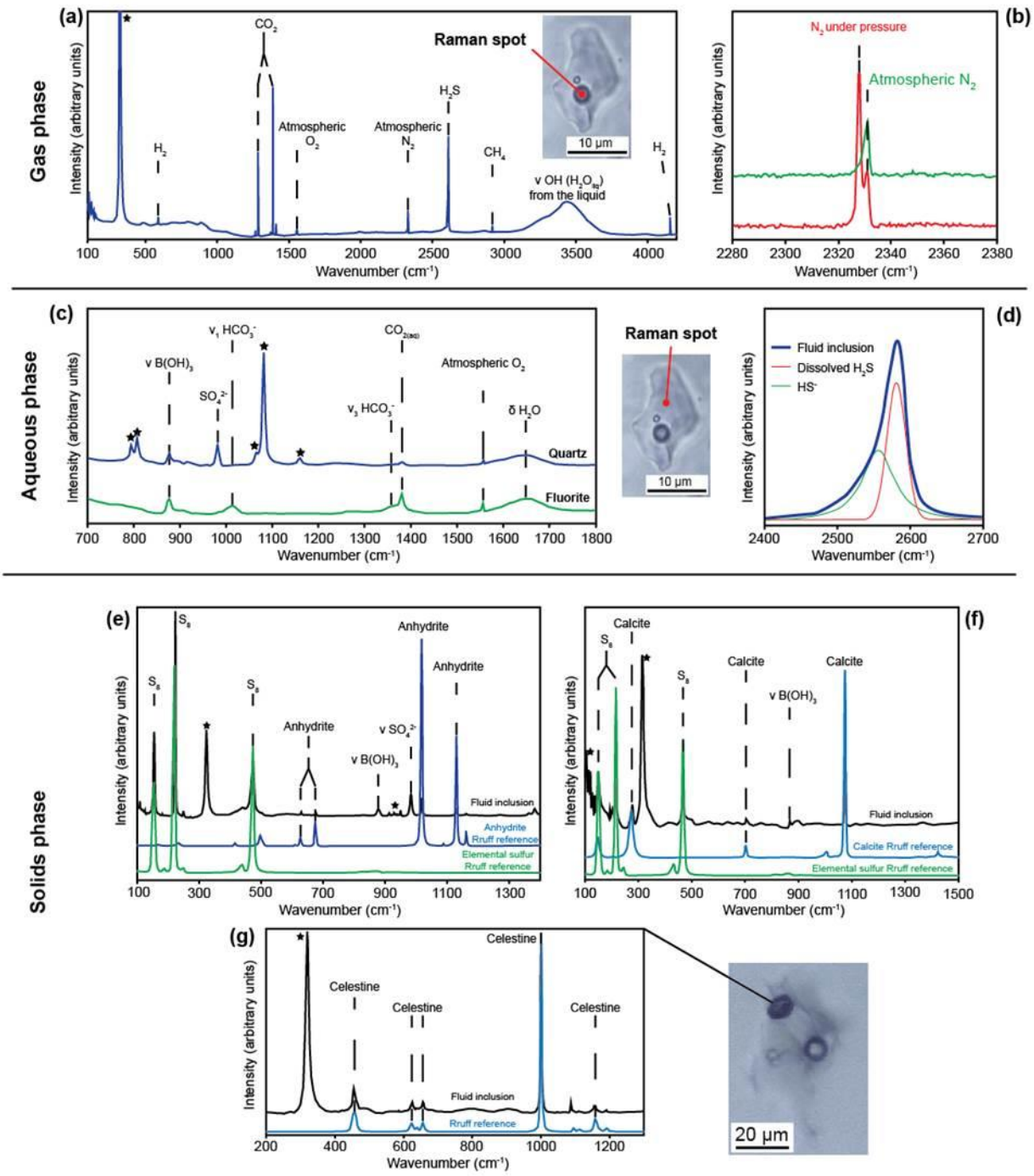

848

849

Figure 6

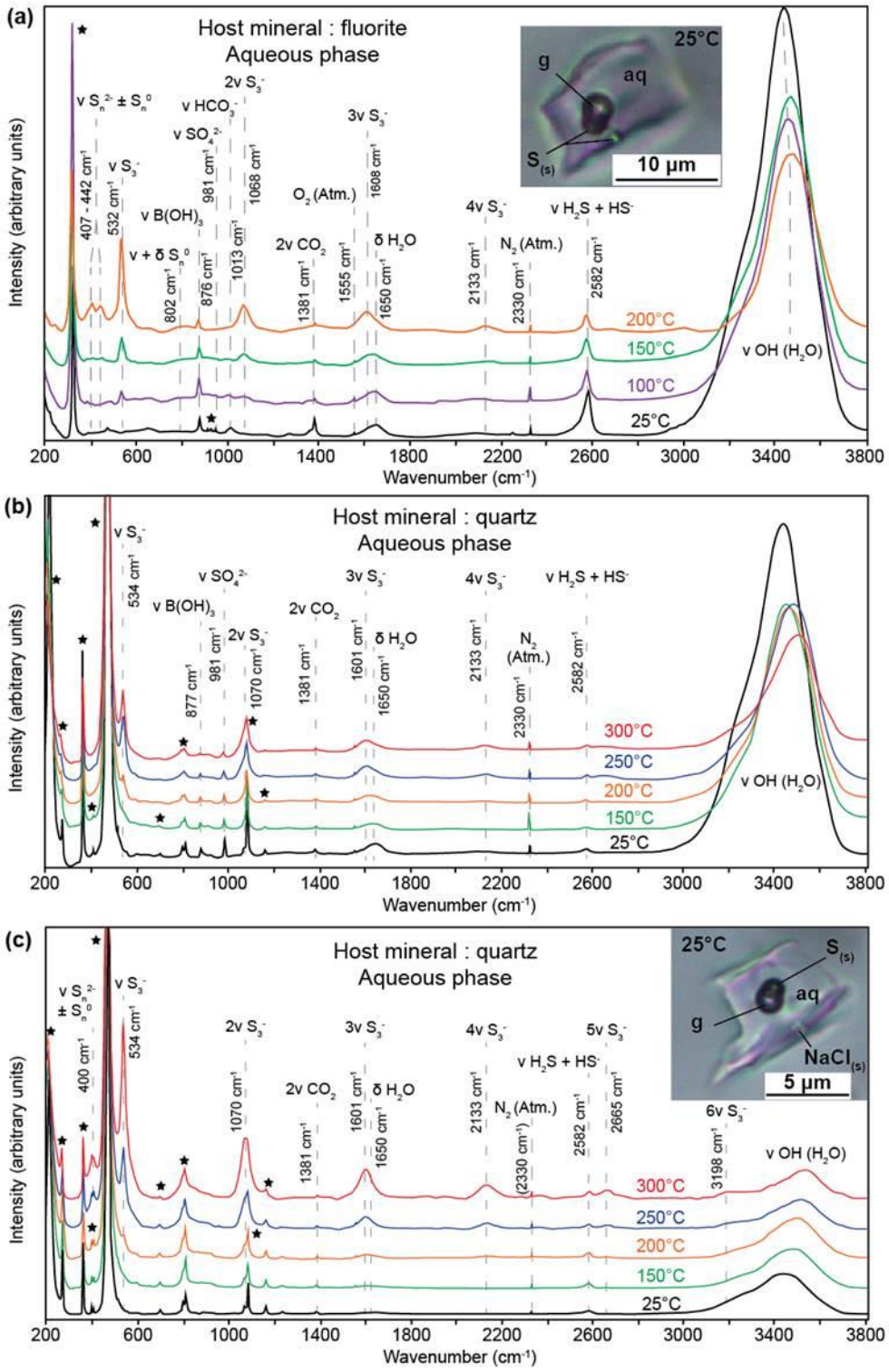
(a)
Host mineral : fluorite
Aqueous phase
25°C
g
aq
S(s)
10 µm
Intensity (arbitrary units)
Wavenumber (cm-1)
200°C
150°C
100°C
25°C
(b)
Host mineral : quartz
Aqueous phase
300°C
250°C
200°C
150°C
25°C
(c)
Host mineral : quartz
Aqueous phase
NaCl(s)
5 µm
300°C
250°C
200°C
150°C
25°C

853 **Figure 7**

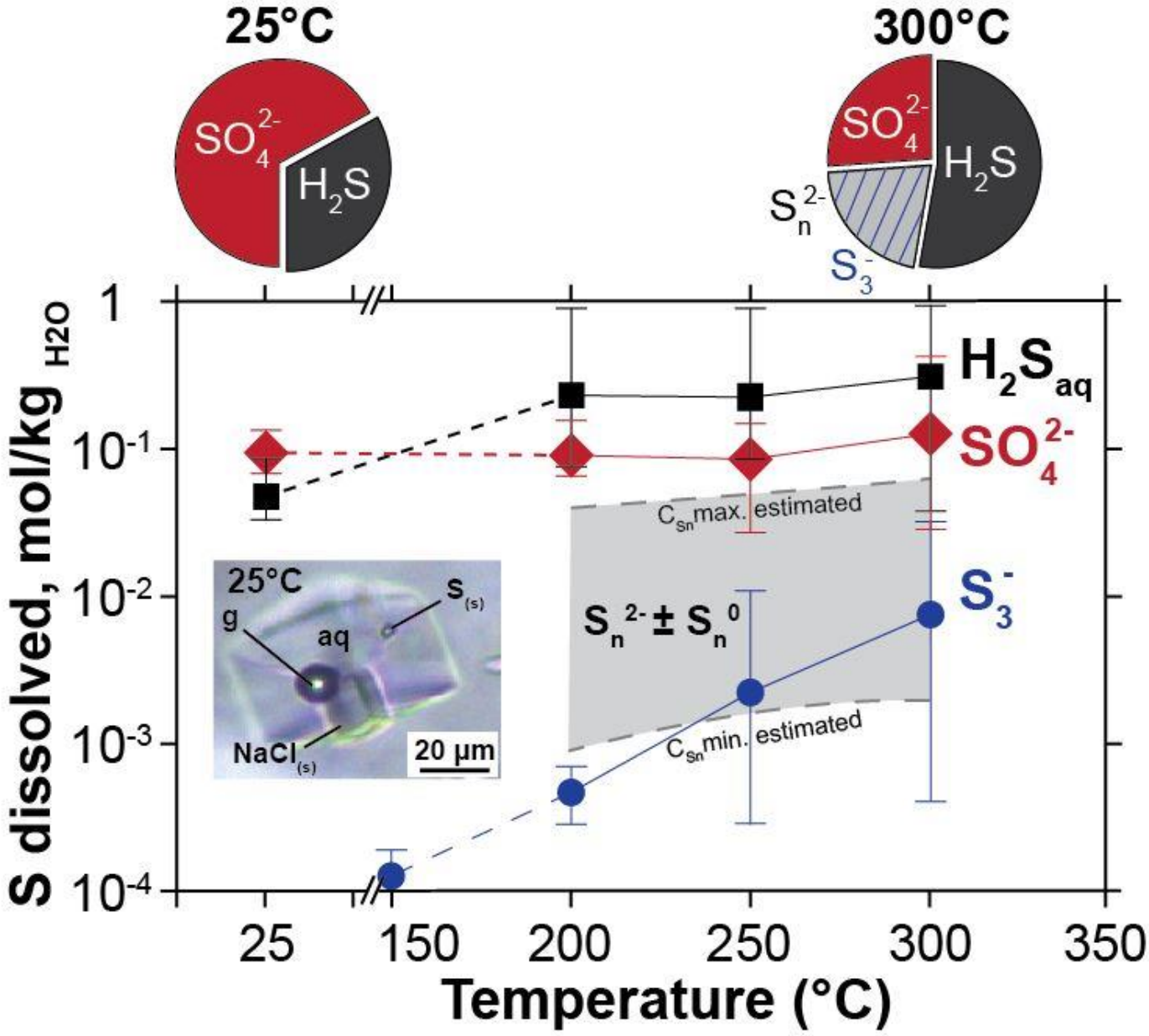

854

855

856 **Figure 8**

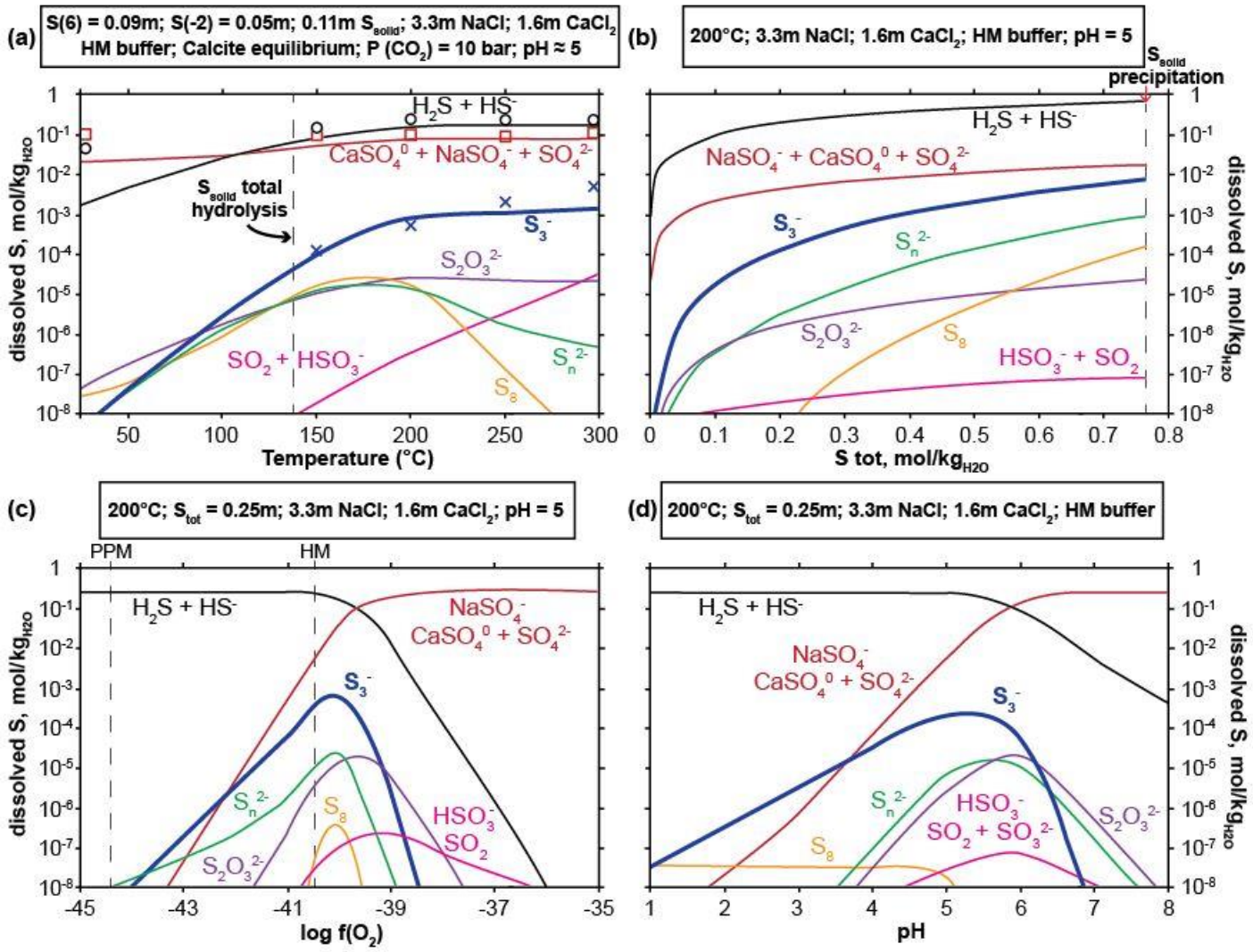

857

858

859 **Figure 9**

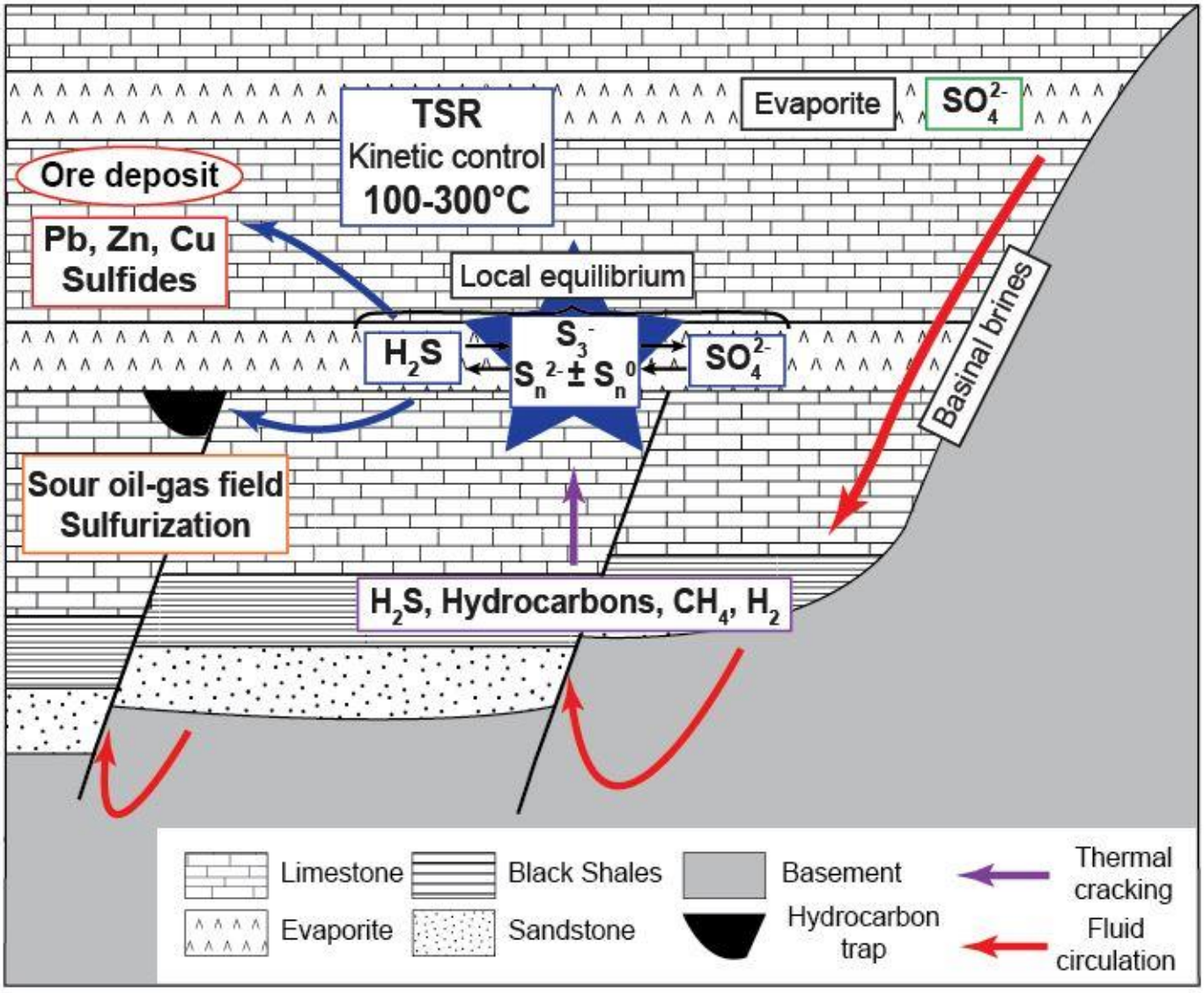

860

861

Table 1

Host mineral	Fluid Inclusion	T (°C)	A S_3^-/ A H_2O	[S_3^-] (mol/kg H_2O)	A SO_4^{2-}/ A H_2O	[SO_4^{2-}] (mol/kg H_2O)	A H_2S/ A H_2O	[H_2S] (mol/kg H_2O)
Quartz	**So. 10 t1**	25	-	-	0.0020	1.06×10^{-1}	0.0009	4.80×10^{-2}
		200	0.0057	6.58×10^{-4}	0.0039	1.55×10^{-1}	0.0009	7.72×10^{-2}
		250	0.0097	1.05×10^{-3}	0.0039	1.51×10^{-1}	0.0013	1.14×10^{-1}
		300	0.0312	2.51×10^{-3}	0.0053	1.96×10^{-1}	0.0024	1.55×10^{-1}
Quartz	**So. 10 t3**	25	-	-	0.0015	7.64×10^{-2}	0.0007	3.53×10^{-2}
		200	0.0027	3.10×10^{-4}	0.0019	7.63×10^{-2}	0.0012	1.06×10^{-1}
		250	0.0125	1.36×10^{-3}	0.0018	7.04×10^{-2}	0.0021	1.80×10^{-1}
		300	0.0199	1.61×10^{-3}	0.0008	2.87×10^{-2}	0.0021	1.32×10^{-1}
Quartz	**So. 10 t4**	25	-	-	0.0020	1.01×10^{-1}	0.0008	4.24×10^{-2}
		200	0.0028	2.91×10^{-4}	0.0031	1.11×10^{-1}	0.0015	1.25×10^{-1}
		250	0.0112	1.05×10^{-3}	0.0038	1.26×10^{-1}	0.0016	1.18×10^{-1}
		300	0.0068	4.49×10^{-4}	0.0021	6.53×10^{-2}	0.0007	3.75×10^{-2}
Quartz	**So. 10 t5**	25	-	-	0.0013	6.81×10^{-2}	0.0009	4.67×10^{-2}
		200	-	-	0.0020	8.09×10^{-2}	0.0027	2.47×10^{-1}
		250	0.0142	1.55×10^{-3}	0.0011	4.43×10^{-2}	0.0014	1.20×10^{-1}
		300	0.0068	5.47×10^{-4}	0.0008	3.01×10^{-2}	0.0021	1.37×10^{-1}
Quartz	**So. 10 t6**	25	-	-	0.0020	1.06×10^{-1}	0.0010	5.11×10^{-2}
		200	0.0030	3.46×10^{-4}	0.0019	7.79×10^{-2}	0.0012	1.06×10^{-1}
		250	0.0027	2.94×10^{-4}	0.0007	2.75×10^{-2}	0.0015	1.33×10^{-1}
		300	0.0051	4.08×10^{-4}	0.0020	7.60×10^{-2}	0.0013	8.37×10^{-2}
Quartz	**So. 2.4 t1**	200	0.0069	7.12×10^{-4}	-	-	0.0111	8.98×10^{-1}
		250	0.1047	1.09×10^{-2}	-	-	0.0110	9.05×10^{-1}
		300	0.3842	2.91×10^{-2}	-	-	0.0148	9.05×10^{-1}
Fluorite	**So. 10.1 t2**	25	-	-	0.0025	1.32×10^{-1}	0.0017	8.40×10^{-2}
		200	-	-	0.0018	7.37×10^{-2}	0.0019	1.69×10^{-1}
		250	0.0073	7.87×10^{-4}	0.0029	1.14×10^{-1}	0.0017	1.48×10^{-1}
		300	0.0391	3.32×10^{-3}	0.0056	2.58×10^{-1}	0.0050	3.10×10^{-1}
Fluorite	**So. 10.1 t1**	25	-	-	0.0018	9.26×10^{-2}	0.0010	5.09×10^{-2}
		200	0.0043	4.97×10^{-4}	0.0024	9.74×10^{-2}	0.0014	1.31×10^{-1}
		200	0.0040	4.63×10^{-4}	0.0015	6.09×10^{-2}	0.0026	2.32×10^{-1}
Fluorite	**So. 10.1 t3**	250	0.0091	9.92×10^{-4}	0.0013	4.93×10^{-2}	0.0010	8.68×10^{-2}
		300	0.0311	2.51×10^{-3}	0.0033	1.22×10^{-1}	0.0015	9.64×10^{-2}
Fluorite	**So. 10.1 t5**	25	-	-	0.0021	1.07×10^{-1}	0.0006	3.30×10^{-2}
Fluorite	**So. 10.1 t6**	25	-	-	0.0014	7.31×10^{-2}	0.0007	3.32×10^{-2}